Numerical study of heat transfer in two phase flows

Master Thesis Report

Ankit Joshi
Student number : 4617053

Faculty of
Process and Energy, 3mE

Energy & Process Technology

Numerical study of heat transfer in two phase flows

by

Ankit Joshi

in partial fulfillment of the requirements for the degree of

Master of Science

in Mechanical Engineering

at the Delft University of Technology,

to be defended publicly on Tuesday August 28, 2018 at 02:00 PM.

Thesis committee:	Prof. dr. ir. B.J. Boersma,	TU Delft, Supervisor
	Dr. ir. Hassan Nemati,	TU Delft, Supervisor
	Dr. ir. W.P. Breugem,	TU Delft
	Dr. ir. R. Pecnik,	TU Delft

This thesis is confidential and cannot be made public until August 28, 2018.

Report number: 2907

Acknowledgement

I would like to thank my supervisors Prof.dr.ir. B.J. Boersma and Dr.ir. Hassan Nemati for guiding me throughout this thesis. This work was simply not possible without the continuous guidance and supervision of Dr.ir. Hassan Nemati. A special thanks to Dr.ir. W.P. Breugem and Dr.ir. R. Pecnik for taking out some of their valuable time for being a member of my thesis committee. I would also like to thank Prof.Dr.-Ing.habil. Bernhard Weigand from the University of Stuttgart for sharing his work on “Numerical study of the temperature field of unsteady moving droplets and of the surrounding gas”. Finally, thanks to my family and friends for providing me with enough emotional and financial support during my studies in the Netherlands.

Ankit Joshi
August, 2018

Summary

Heat transfer in multiphase flow plays an important role in nature and in numerous industries such as petrochemical, automotive, food processing, ocean engineering etc. It is becoming increasingly crucial to design more efficient industrial systems to reduce the environmental impact of industrial activities because of global warming and growing awareness about sustainability. To design these efficient systems it is important to thoroughly understand the details of heat transfer in multiphase flow.

This thesis follows the method of Direct Numerical Simulation (DNS) to provide a detailed physical insight of the fluid motion and heat transfer in the model. To accurately model the two phase flow the Coupled Level Set Volume Of Fluid (CLSVOF) method is used. The main advantage of using the CLSVOF method is that it can accurately capture the interface geometry and it has excellent volume conservation capability. The work presented here is an extension to an in-house code developed at TU Delft for Direct Numerical Simulation of two-phase flows using the CLSVOF method. The existing code has been thoroughly validated for the fluid and interface motion but the validation of the heat transfer model remains an unaccomplished task till now. Therefore, the main objective of this thesis is to validate the heat transfer model and then to study the heat transfer in droplets coalescence using this model.

The validation of the heat transfer model was accomplished by calculating the Nusselt number distribution over a bubble surface and comparing it to the available literature. Both the model results and the information from the literature showed very good agreement with each other. After completing the model validation, this model was used to study the heat transfer phenomenon between two coalescing droplets and the surrounding fluid. The results of the droplets coalescence are as per the expectations and are discussed in detail in this thesis. In the process of doing these analyses different ways of calculating the local Nusselt number and the global Nusselt number have been discussed. The validation of the heat transfer model and the analysis done for the case of coalescing droplets paves the way for conducting more complex heat transfer analysis in two-phase flows using this model.

Contents

List of Symbols

Abbreviations

CLSVOF	Coupled Level Set Volume Of Fluid
LS	Level set
VOF	Volume of fluid

Symbols

μ	Dynamic viscosity
∇	Gradient
Γ	Interface
λ	Conductivity
Φ	Level Set function
Ψ	Volume of fluid function
ρ	Density
σ	Surface tension
τ	Shear Stress
A	Area
c	Concentration
C_p	Heat capacity
D	Bubble diameter
d	Diffusivity
g	Gravitational acceleration
h	Grid dimension
h_c	Heat transfer coefficient
I	Identity matrix
k	Interface curvature
L	Length scale
m	Mass
$\mathbf{n}$	Interface normal vector
$\hat{\mathbf{n}}$	Interface normal unit vector
p	Pressure
q	Heat flux
$\dot{q}$	Heat transfer rate
R	Material Property

S	Surface area
s	Triangle side
T	Temperature
t	Time
U	Velocity scale
$\mathbf{u}$	Velocity vector
x	Area expansion factor

Subscripts

avg	Average
c	Continuous phase property
d	Dispersed phase property
i, j	Cell indices

Dimensionless numbers

Eo	Eotvos number
M	Morton number
Nu	Nusselt number
Pr	Prandtl number
Re	Reynolds number
Sc	Schmidt number
Sh	Sherwood number
We	Weber number

1 Introduction

Since the beginning, we as humans have always tried to learn from nature and then use these learnings for our benefits. Many of these learnings which were discovered centuries and millenniums ago are still in use to make this world a better place to live and exploring other worlds for human habitation. Although it can definitely be argued if today's world is a better place or worse place to live than it was millenniums ago but there is one thing for sure that in the recent centuries we have seen a lot of changes in our surrounding and all these changes are attributable to our science and engineering prowess.

One of the very important phenomena observed in the nature is the heat transfer in multiphase flows. It is interesting and important to understand this phenomenon in detail because of it's various application areas. A thorough explanation of this phenomenon and how it can be modelled is given in the next few sections of this chapter.

1.1 Heat transfer in multiphase flow

As the name suggests, heat transfer in multiphase flow deals with the flow of thermal energy taking place between more than one phases. This thesis specifically covers the area of two phase flows where the two phases are immiscible fluids, with one of it in the dispersed phase and the other one in the continuous phase.

There are a plethora of examples where such kind of flows are present in nature and in man-made things. One of which is shown in the figure below.

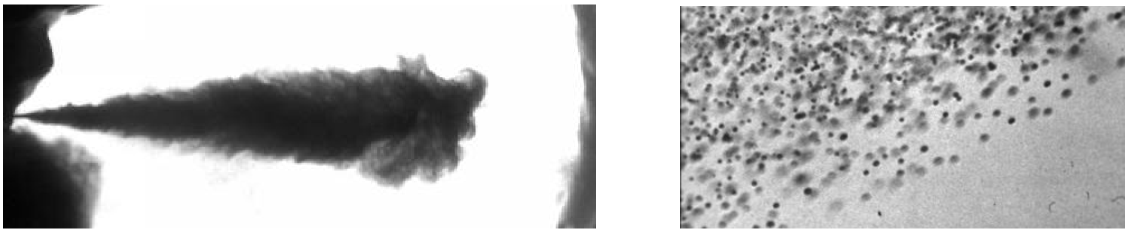

(a) Diesel fuel spray

(b) Droplets at the edge of the diesel spray

Figure 1.1: Diesel fuel spray. Image source: //icel.tkk.fi/research/Common_Rail.html

In Fig.1.1b, it can be seen that the fuel drops are dispersed very finely in the air. A detailed knowledge about the heat transfer between the air and the diesel drops can be used to optimize the combustion characteristics in the combustion chamber to reduce emissions, improve efficiency etc. A similar analysis can be done for a variety of applications to achieve the desired results. Other examples of multiphase flows include flow in condenser/evaporators, aeration of water for treatment, steam turbines, filtration and separation systems.

In this thesis, the method of Direct Numerical Simulation (DNS) was used to model the fluid motion and heat transfer in two-phase flow. In DNS the governing equations of the fluid and energy flow are solved as it is on a continuum scale without any assumptions. The main advantage of using DNS over other numerical methods is that it can give a very detailed and accurate information about the velocity and temperature field of the flow. However, DNS has its disadvantages when it comes to the efficiency or speed of the model. This is the reason why DNS is used only for limited applications in the industry.

To get the information about the heat transfer in the flow, first the equations of fluid flow are solved independently and then from the knowledge of the velocity field, temperature field is calculated at every time step . This means that the energy equation is dependent upon the fluid flow equations but not vice-versa. This one-way coupling between the flow field and the temperature field is adopted to simplify the model and can be applied where the temperature is not affecting the flow field, for e.g. in flows where the viscosity is temperature independent. Therefore all the material properties are considered as constants in this model. Also, only the conductive and convective transport of energy is considered in this model and any radiation/energy generation effects are neglected. Any phase change process such as evaporation and condensation are also not included in this model. More will be discussed about the governing equations in the next chapter.

An important point to note here is that all the equations are solved in the continuum scale. This means that the minimum physical length scale of the model is much larger than the mean free path of the constituent molecules. At the continuum scale, the material properties can be defined at any point in the fluid and these properties vary discontinuously at the interface.

1.2 Modelling of multiphase flow

Modelling of multiphase flow with different material properties in the presence of an interface and surface tension is a cumbersome process compared to the modelling of single phase flows. Over the years several methods to model multiphase flows have been developed. Some of the most widely used methods to model these flows are front tracking, level set and volume of fluid method.

Front tracking method uses marker particles to track the interface position. The main advantage of the front tracking method is that the interface can be accurately represented and there is no numerical coalescence or breakup of the interface. Its disadvantages include the requirement of a dynamic restructuring of the marker particles and inefficient volume conservation.

In the case of the Level set method, a level set function (Φ) is defined over the domain. This level set function is a distance function to the interface. This means that it has zero value at the interface and it is defined as positive distance inside the interface and negative distance outside the interface. The main advantage of Level set method is that

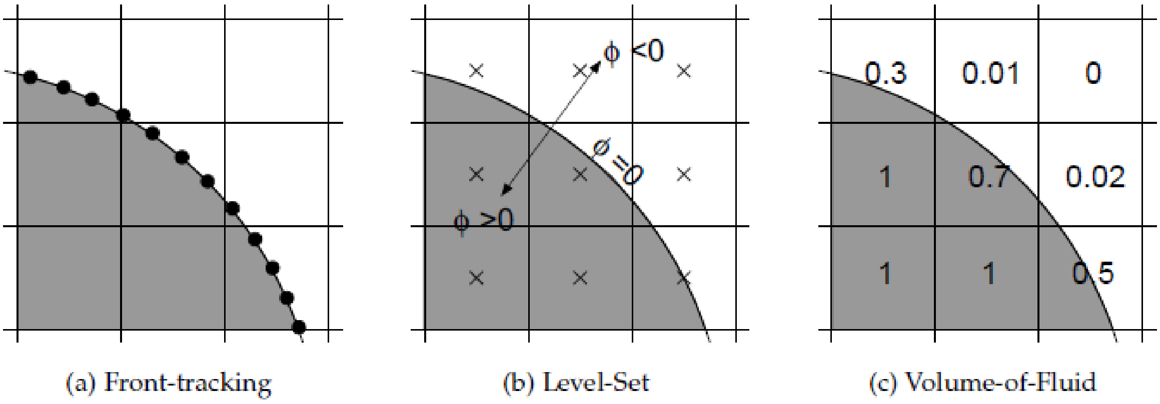

(a) Front-tracking (b) Level-Set (c) Volume-of-Fluid

Figure 1.2: Some of the methods to model multiphase flow [1]

the interface position, interface normal and the interface curvature can be easily extracted from the level set values. However, this method also has similar disadvantages as that of the front tracking method i.e. re-initialization of the level set function is required after every time step and it has poor volume conservation.

In the volume of fluid (VOF) method, a VOF function is defined for the domain. Value of this VOF function is equal to the volume fraction of the dispersed phase in that particular cell. So if the cell is completely filled up by the dispersed phase, the value of the VOF function is 1. If it's completely filled up with the continuous phase then the VOF function has a value of 0 and if the cell contains both the phases then it's value is between 0 and 1. The main advantage of using the VOF method is that it has excellent volume conservation but it's not possible to extract interface topologies from the VOF function since it only represents the volume fraction present in the cell and tells nothing about the distribution of the fluid inside the cell.

Therefore, none of the above methods is a perfect method for the modelling of multiphase flow. So it is quite common to use a combination of different methods, where the advantage of one method compensates for the disadvantage of the other method. This thesis uses a combination of the Level Set and Volume of Fluid method developed by Sussman and Puckett [2]. This method is named as Coupled Level Set Volume Of Fluid(CLSVOF) method and has combined advantages of both LS and VOF method i.e. easy extraction of the interface geometry and good volume conservation.

In this model, a uniform and fixed grid was used to solve the governing equations. Although a nonuniform and deformable grid fixed to the interface seems to be a better choice for capturing the details of the thermal boundary layer but using a non-uniform and deformable grid can get very complex and expensive in case of dispersed multiphase flow with the CLSVOF method.

The original model used in this thesis was developed by Coyajee [1] and Kwakkel [3] based on the CLSVOF method of Sussman and Puckett [2]. A brief overview of the original model is given in the next chapter along with the governing equations which were used to model the multiphase flow.

1.3 Outline of this thesis

The main objective of this thesis is to validate the heat transfer model and then use this model to understand the physics behind the heat transfer between bubbles and liquid for different flow configurations.

This thesis is divided into different chapters. The next chapter will discuss the governing equations and a brief overview of the complete model. Chapter 3 is completely dedicated to the validation of the energy equation and chapter 4 discusses the heat transfer between two coalescing droplets and a surrounding fluid. Finally, this thesis ends with chapter 5, where conclusions and recommendations for the future work are given.

2 Governing equations and Model overview

This chapter will give a brief overview of the model developed by Coyajee [1] and Kwakkel [3]. Starting from the governing equations of the flow to the numerical procedures used to solve these governing equations. The fluids in this model are assumed to be incompressible Newtonian fluids with constant material properties.

2.1 Governing equations for the fluid phases

The governing equations used in this model are simply the well known physical laws represented in the terms of differential equations so that after solving these equations it is possible to acquire a detailed information of the flow. These physical laws are,

Conservation of mass (Continuity equation):

$$\nabla \cdot \mathbf{u} = 0 \tag{2.1}$$

Conservation of momentum (Navier Stokes equation):

$$\frac{\partial \mathbf{u}}{\partial t} + \mathbf{u} \cdot \nabla \mathbf{u} = -\frac{1}{\rho}\nabla p + \frac{1}{\rho}\nabla \cdot (\mu(\nabla \mathbf{u} + \nabla \mathbf{u}^T)) + \mathbf{g} \tag{2.2}$$

Conservation of energy (Energy equation):

$$\frac{\partial T}{\partial t} + \mathbf{u} \cdot \nabla T = \frac{1}{\rho C_p}\nabla \cdot (\lambda \nabla T) \tag{2.3}$$

In the above equations, all the vectors are presented with bold letters. From the Eq. 2.3, it is evident that only the conductive and convective heat transports are considered in this model and heat generations effects are excluded.

For the continuity of fluid velocity and continuity of stresses at the interface, the conditions given by Batchelor [4] and Landau and Lifshitz [5] are applied at the interface. These conditions are given in the form of Eq. 2.4 and Eq. 2.5, where Γ represents the jump across the interface, k is the interface curvature, σ represents the surface tension coefficient and $\mathbf{n}$ is the interface normal vector.

$$[\mathbf{u}]_\Gamma = 0 \tag{2.4}$$

$$[(-pI + \tau) \cdot \mathbf{n}]_\Gamma = -\sigma k \mathbf{n} \tag{2.5}$$

Kang et al. [6] showed that if the viscosity is regularized over the interface, the derivatives of velocity becomes continuous at the interface. Although this assumption makes this model a little bit less accurate but it gives a huge advantage by decoupling the jump conditions of pressure and velocity. Using this simplification Eq. 2.5 modifies to,

$$[p]_\Gamma = \sigma k \tag{2.6}$$

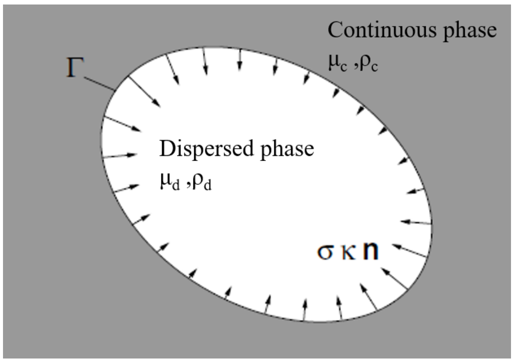

Figure 2.1: Description of fluid phases with the interface. Surface tension force is acting in the direction of the normal vector. Figure adapted from [1]

2.2 Interface description

As already discussed in the last chapter, this thesis uses the CLSVOF method of Sussman and Puckett [2]. In this method, both the level set function and the volume of fluid function are used to model the multiphase flow. The Level Set function (Φ) is a distance function to the interface such that it is positive inside the dispersed phase and negative in the continuous phase. The value of the Level Set function at the interface is zero. Since the interface is a material property of the flow, it's motion can be described in terms of the Level Set function as,

$$\frac{\partial \Phi}{\partial t} + \mathbf{u} \cdot \nabla \Phi = 0 \tag{2.7}$$

In a similar way, the governing equation of the Volume of Fluid function (Ψ) can be described as the conservation law for the volume fraction and is given by Eq. 2.8. Eq. 2.7 and Eq. 2.8 are solved in combination from the known velocity field at every time step to capture the interface during the simulation.

$$\frac{\partial \Psi}{\partial t} + \mathbf{u} \cdot \nabla \Psi = 0 \tag{2.8}$$

From the definition of the Level Set function, the fluid properties can be defined by Eq. 2.9. Here R represents any thermal or physical property of the fluid and the subscript c/d represents the continuous/dispersed phase respectively.

$$R = R_c(1 - H(\Phi)) + R_d H(\Phi) \tag{2.9}$$

The Heaviside function $H(\Phi)$ used in Eq. 2.9 is defined as,

$$H(\Phi) = \begin{cases} 1, & \text{if } \Phi > 0 \\ 0, & \text{otherwise} \end{cases} \tag{2.10}$$

It is clear that the Eq. 2.10 represents a sharp jump in the material property over the interface but for calculating smoothly varying properties over the interface such as viscosity, the Heaviside function is replaced by a new continuous function $H_\alpha(\Phi)$, this function is smoothly varying over a width of 2α across the interface. In this model, α was chosen as $3h/2$, where h is the mesh width.

$$H_\alpha(\Phi) = \begin{cases} 0 & \text{if } \Phi < -\alpha \\ \frac{1}{2}(1 + \frac{\Phi}{\alpha} + \frac{1}{\pi} sin(\frac{\pi\Phi}{\alpha})) & \text{if } |\Phi| \leq \alpha \\ 1 & \text{if } \Phi > \alpha \end{cases} \tag{2.11}$$

2.3 Dimensionless parameters

The governing equations in this model are solved in non-dimensional forms. These non-dimensional equations can be formed by using appropriate scales for the flow. Eq. 2.2, Eq. 2.3 and Eq. 2.6 can be non-dimensionalized by taking L as the characteristic length scale, U as velocity scale, continuous phase properties as the property scale and initial temperature difference between the phases as the temperature scale. These new non-dimensional parameters are:

$$\begin{array}{lll} \mathbf{x}' = \mathbf{x}/L, & \mathbf{u}' = \mathbf{u}/U & t' = t/(L/U) \\ \rho' = \rho/\rho_c & \mu' = \mu/\mu_c & p' = p/(\rho_c U^2) \\ \lambda' = \lambda/\lambda_c & {C_p}' = C_p/C_{p_c} & T' = (T - T_c)/(T_d - T_c) \end{array}$$

After using the above given dimensionless parameters and dropping the primes, the new dimensionless equations are given as,

$$\frac{\partial \mathbf{u}}{\partial t} + \mathbf{u} \cdot \nabla \mathbf{u} = -\frac{1}{\rho}\nabla p + \frac{1}{\rho Re}\nabla \cdot (\mu(\nabla \mathbf{u} + \nabla \mathbf{u}^T)) + \frac{\hat{\mathbf{g}}}{Fr} \tag{2.12}$$

$$\frac{\partial T}{\partial t} + \mathbf{u} \cdot \nabla T = \frac{1}{\rho C_p Re Pr}\nabla \cdot (\lambda \nabla T) \tag{2.13}$$

$$[p]_\Gamma = \frac{k}{We} \tag{2.14}$$

In the above equations, the dimensionless numbers are the Reynolds number (Re), Froude number (Fr), Prandtl number (Pr) and Weber number (We). These dimensionless numbers are defined as,

$$Re = \rho_c U L/\mu_c \qquad Fr = U^2/gL \tag{2.15}$$

$$Pr = \mu_c C_{p_c}/\lambda_c \qquad We = \rho_c L U^2/\sigma \tag{2.16}$$

Similarly, the dimensionless fluid properties can be calculated using Eq. 2.17. Here r is the property ratio and is defined as $r = R_d/R_c$. For continuously varying properties $H(\Phi)$ can be replaced by $H_\alpha(\Phi)$.

$$R = 1 + (r-1)H(\Phi) \tag{2.17}$$

2.4 Discretization of the governing equations

The equations are discretized on a uniform Cartesian grid with a staggered arrangement of variables, where the scalars and markers functions (LS and VOF) are defined at the cell centres and the velocity components are located at the cell faces. Both the Navier Stokes equation and the energy equation are integrated using the second order Adams-Bashforth scheme. The main difference in the existing code from the original code developed by Coyajee [1] and Kwakkel [3] is the implementation of the energy equation by Talebanfard and Boersma [7] and the introduction of an FFT-based fast Poisson solver developed by Dodd and Ferrante [8].

For the discretization of the Navier Stokes, first an approximate velocity is calculated without any pressure term using Eq. 2.18

$$\frac{\mathbf{u}^* - \mathbf{u}^n}{\Delta t} = \frac{3}{2}\mathbf{RU}^n - \frac{1}{2}\mathbf{RU}^{n-1} + \frac{\hat{\mathbf{g}}}{Fr} \tag{2.18}$$

where $\mathbf{RU}$ is defined as,

$$\mathbf{RU}^n = -\nabla\cdot(\mathbf{u}^n\mathbf{u}^n) + \frac{1}{\rho^{n+1}Re}\nabla\cdot\left(\mu^{n+1}(\nabla\mathbf{u}^n + (\nabla\mathbf{u}^n)^T)\right) \tag{2.19}$$

The fluid properties in Eq. 2.19 are obtained from the new interface position at $n+1$ time step. The correct velocity field can be obtained using Eq. 2.20,

$$\frac{\mathbf{u}^{n+1} - \mathbf{u}^*}{\Delta t} = -\frac{1}{\rho^{n+1}}\nabla p^{n+1} \tag{2.20}$$

The new velocity field at time step $n+1$ should also satisfy the divergence free condition of the continuity equation. Therefore, taking the divergence of Eq. 2.20 on both sides gives,

$$\nabla\cdot\left(\frac{1}{\rho^{n+1}}\nabla p^{n+1}\right) = \frac{1}{\Delta t}\nabla\cdot\mathbf{u}^* \tag{2.21}$$

In Eq. 2.21 density is not constant throughout the computational domain. This makes it difficult to solve the pressure Poisson equation using the direct solvers. Iterative solvers are generally used to solve these kinds of variable coefficient Poisson equations but the issue with the iterative solvers is that they are very slow as compared to the direct solvers. Another advantage of using direct solvers is that they satisfy the divergence free condition up to the machine precision, which also improves the accuracy of the solution. The method developed by Dodd and Ferrante [8] converts the Eq. 2.21 to a constant coefficient Poisson equation and solve it using an FFT based fast Poisson solver. The idea is to split the variable LHS term of Eq. 2.21 into a constant implicit term and a variable explicit term. This is given as,

$$\frac{1}{\rho^{n+1}}\nabla p^{n+1} \rightarrow \frac{1}{\rho_0}\nabla p^{n+1} + \left(\frac{1}{\rho^{n+1}} - \frac{1}{\rho_0}\right)\nabla \hat{p} \tag{2.22}$$

where $\rho_0 = min(\rho_c, \rho_d)$ for numerical stability [9] and $\hat{p} = 2p^n - p^{n-1}$ for better physical accuracy of the solution [8]. Using the Eq. 2.22, the velocity field at the new time step can be calculated by,

$$\mathbf{u}^{n+1} = \mathbf{u}^* - \Delta t\left(\frac{1}{\rho_0}\nabla p^{n+1} + \left(\frac{1}{\rho^{n+1}} - \frac{1}{\rho_0}\right)\nabla \hat{p}\right) \tag{2.23}$$

One might notice that there is no mention of the surface tension force in the description of Navier Stokes equation. This is because the surface tension force is included in the pressure gradient term as,

$$\left(\frac{\partial p}{\partial x}\right)_{i+\frac{1}{2}} = \frac{p_{i+1} - p_i - [p]_\Gamma}{\Delta x} \tag{2.24}$$

where,

$$[p]_\Gamma = \begin{cases} k/We & \text{if } \Phi_i \leq 0 \text{ and } \Phi_{i+1} > 0 \\ -k/We & \text{if } \Phi_i > 0 \text{ and } \Phi_{i+1} \leq 0 \\ 0 & \text{otherwise} \end{cases} \tag{2.25}$$

The energy equation is also integrated using the second order Adams Bashforth method as given below,

$$\frac{T^{n+1} - T^n}{\Delta t} = \frac{3}{2}RT^n - \frac{1}{2}RT^{n-1} \tag{2.26}$$

where RT is given by,

$$RT^n = -\nabla \mathbf{u}^n T^n + \frac{1}{\rho^{n+1}C_p^{n+1}RePr}\nabla \cdot (\lambda^{n+1}\nabla T^n) \tag{2.27}$$

The convective term in Eq. 2.27 is discretized using Van Leer flux limiter [10] to ensure smooth solutions at sharp temperature gradients.

Some of the material properties are required to be calculated at the cell faces, such as density in Eq. 2.19 and conductivity in Eq. 2.27. In the vicinity of the interface these properties are calculated using a weighted harmonic average method proposed by Liu et al. [11]. For eg. to calculate a property R at $i + 1/2$ position, the following equations are used,

$$R_{i+1/2} = R_i\theta + R_{i+1}(1 - \theta) \tag{2.28}$$

$$\theta = \frac{|\Phi_i|}{|\Phi_i| + |\Phi_{i+1}|} \tag{2.29}$$

For calculating the cell centre values of the material properties like density and specific heat in Eq. 2.27, the VOF function was used.

$$R_i = R_d\Psi_i + R_c(1 - \Psi_i) \tag{2.30}$$

2.5 Model overview

The existing model developed by Coyajee [1] and Kwakkel [3] has been thoroughly validated for the interface description, droplets coalescence, and droplet-laden turbulent flow. To prevent the numerical coalescence of the bubbles, a multiple marker method was developed by Coyajee [1]. Several methods were adopted in this model to improve its efficiency, such as parallelization using three-dimensional domain decomposition approach, implementation of a local multiple marker method based on a master/slave technique and using an FFT based pressure Poisson equation solver by Nemati et al. [12]. All this work is a proof of the accuracy and robustness of this model to accurately represent the interface, implementation of the jump conditions at the interface, model bubble coalescence and breakup, and model turbulent bubbly flow while being reasonably efficient at the same time.

With the existing heat transfer model, some of the work has already been presented by Talebanfard and Boersma [7] on the analysis of heat transfer in colliding droplets but the validation of the heat transfer model still remains an unaccomplished task. Most of the available literature in the field of heat/mass transfer in multiphase flow [13, 14, 15] generally concerns with the global heat/mass exchange between the phases and doesn't discuss the distribution of heat transfer over the interfaces, which is required for the complete and accurate validation of the heat transfer model.

It is important to mention the work of Cerqueira et al. [16] in this thesis because it gave the main direction in performing the validation of the heat transfer model. Cerqueira et al. [16] studied the heat transfer between a rising bubble and surrounding fluid using only the VOF approach and compared the distribution of Nusselt number over the bubble surface with the results of Oellrich et al. [17]. Since only the VOF approach was followed in [16] it was difficult to exactly track the interface even with very high mesh refinement and hence it was difficult to accurately calculate the local Nusselt number at the interface. Therefore, the comparison of the local Nusselt number in [16] with Oellrich et al. [17] was performed only on the basis of a normalized Nusselt number distribution and the final validation of the model was done using the global Nusselt number values. However, in the model developed by Coyajee [1] and Kwakkel [3] it is much easier to track the interface using the CLSVOF method. Therefore the local Nusselt number can be accurately calculated. This procedure of Nusselt number calculation and the validation of the model is thoroughly explained in the next chapter.

3 Model validation

Validation of a model is always a requirement prior to using that model for analyzing different flow phenomena. This model is validated using the results given by Oellrich et al. [17] for steady state mass transfer between a stationary spherical bubble and moving fluid. Due to the similarity between the governing equations of mass transfer and heat transfer these results [17] can be used to validate the model.

Similarity between Eq. 3.1 for mass transfer and Eq. 2.13 for heat transfer is quite evident and it is clear that the Prandtl number (Pr) in heat transfer is analogous to the Schmidt number (Sc) in mass transfer. Similarly, the Nusselt number (Nu) in heat transfer is analogous to the Sherwood number (Sh) in mass transfer. In Eq. 3.1, c represents the specie concentration and d represents the diffusivity.

$$\frac{\partial c}{\partial t} + \mathbf{u} \cdot \nabla c = \frac{1}{ReSc} \nabla \cdot (d \nabla c) \tag{3.1}$$

The Local Nusselt number can be defined as the dimensionless temperature gradient normal to the bubble surface, as given by Eq. 3.2. The average Nusselt number is calculated by averaging the local Nusselt number over the bubble surface area. This is given by Eq. 3.3 where S represents the bubble surface.

$$Nu = -\frac{\partial T}{\partial n} \tag{3.2}$$

$$Nu_{avg} = \frac{\displaystyle\int_S Nu dA}{\displaystyle\int_S dA} \tag{3.3}$$

The validation of this model can be completed by comparing the distribution of the Nusselt number and the average value of the Nusselt number over the bubble surface with the results available in Oellrich et al. [17]. It should be noted that if the calculated Nusselt number distribution is correct then it already implies that the average Nusselt number should also be correct provided that the area calculations are done accurately but vice versa is not true.

The most important points to achieve the conditions given in Oellrich et al. [17] were:

1. The bubble should remain spherical.
2. Steady state conditions should be achieved.
3. The bubble should be at a constant temperature.

To simulate the conditions given in Oellrich et al. [17] it was decided to model a constant temperature bubble rising through a fluid medium. The first condition was achieved by selecting the Eotvos number (Eo) and the Morton number (M) such that the bubble remains in the spherical region geometry, as shown by the blue circle in Fig. 3.1. This figure shows different shape regimes for a freely rising bubble/falling drops under gravity. The second condition can be checked by observing the flow properties with time. Finally, the third condition can be very easily achieved by initializing the temperature of the bubble at every time step.

$$Eo = \frac{\Delta\rho g D^2}{\sigma} \qquad\qquad M = \frac{\Delta\rho g \mu_c^4}{\rho_c^2 \sigma^3} \tag{3.4}$$

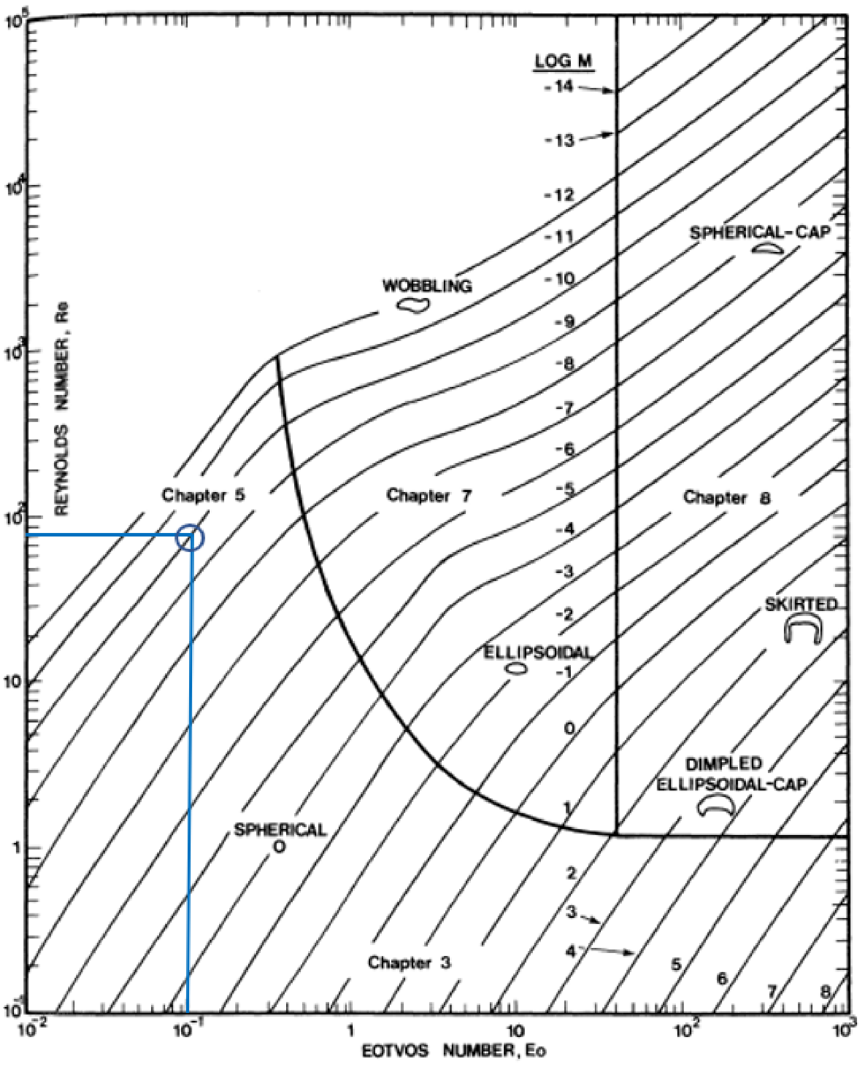

Figure 3.1: Shapes of freely falling/rising dispersed fluid particles under the action of gravity [18]

In the following sections, the discussion will be on the calculation of the interfacial area, calculation procedure for the Nusselt number, geometry and parameters of the model and finally the model validation will be covered.

3.1 Interfacial area calculation

The calculation of the interfacial area is based on the approach followed by Van der Pijl [19] which was used to calculate the VOF function from the LS function. This thesis follows the same approach but for a different outcome i.e. to calculate the interfacial area from the LS function. For an easy description of the procedure, the interfacial area is calculated for a cubical cell of dimension h, therefore this method can be directly implemented in the model since the computational mesh is uniform in all the directions. In this model the interfacial cells can be identified as those cells where $0 < \Psi < 1$.

The idea was to linearize the level set function around the cell centre. By using this linearization it is possible to approximate the interfacial area using a plane. The area of this plane is a function of the LS value and the gradient of LS (or orientation of the plane). The linearization of the LS function around a cell centre x_k is given by:

$$\Phi(y; \Phi, \nabla\Phi, x_k) = \Phi_k + \nabla\Phi \cdot (y - x_k) \tag{3.5}$$

The above linearization can be mapped onto a computational cell with coordinates $(\xi, \eta, \zeta) \in (\frac{-h}{2}, \frac{h}{2})^3$ and the linearization can represented as,

$$\Phi = \Phi_k + \frac{D_\xi \xi + D_\eta \eta + D_\zeta \zeta}{h} \tag{3.6}$$

The 3 axes ξ, η and ζ were chosen such that

$$D_\xi \geq D_\eta \geq D_\zeta \geq 0 \tag{3.7}$$

where,

$$\begin{aligned} D_\xi &= max(|h(\tfrac{\partial\Phi}{\partial x})_k|, |h(\tfrac{\partial\Phi}{\partial y})_k|, |h(\tfrac{\partial\Phi}{\partial z})_k|), \\ D_\zeta &= min(|h(\tfrac{\partial\Phi}{\partial x})_k|, |h(\tfrac{\partial\Phi}{\partial y})_k|, |h(\tfrac{\partial\Phi}{\partial z})_k|), \\ D_\eta &= |h(\tfrac{\partial\Phi}{\partial x})_k| + |h(\tfrac{\partial\Phi}{\partial y})_k| + |h(\tfrac{\partial\Phi}{\partial z})_k| - D_\xi - D_\zeta \end{aligned} \tag{3.8}$$

The choice of the axis restricts the possible topologies of the interfacial surface to only two cases as shown in Fig. 3.2. Due to symmetry, only those cases were discussed here where $\Phi_k \leq 0$. For cells where $\Phi_k > 0$ the same method can be used by changing the value of the LS to $-\Phi_k$. The area of this plane which is inside the computational cell is approximately equal to the area of interface surface present in that cell. Using Eq. 3.6, the values of the LS can be computed at the cell vertices. This is given as,

$$\begin{aligned} \Phi_A &= \Phi_k + \tfrac{D_\xi}{2} + \tfrac{D_\eta}{2} + \tfrac{D_\zeta}{2}, \\ \Phi_B &= \Phi_k + \tfrac{D_\xi}{2} + \tfrac{D_\eta}{2} - \tfrac{D_\zeta}{2}, \\ \Phi_C &= \Phi_k + \tfrac{D_\xi}{2} - \tfrac{D_\eta}{2} + \tfrac{D_\zeta}{2}, \\ \Phi_D &= \Phi_k - \tfrac{D_\xi}{2} + \tfrac{D_\eta}{2} + \tfrac{D_\zeta}{2}, \\ \Phi_E &= \Phi_k + \tfrac{D_\xi}{2} - \tfrac{D_\eta}{2} - \tfrac{D_\zeta}{2}, \end{aligned} \tag{3.9}$$

Each of these vertices can form a pyramid with the interfacial plane which is shown by the shaded region in Fig 3.3. The sides of these pyramids which are emerging from the cell vertices can be given in terms of the LS function, gradient of LS and cell dimension h as shown in Fig. 3.3. From this information the area of the interface can be calculated using Eq. 3.10.

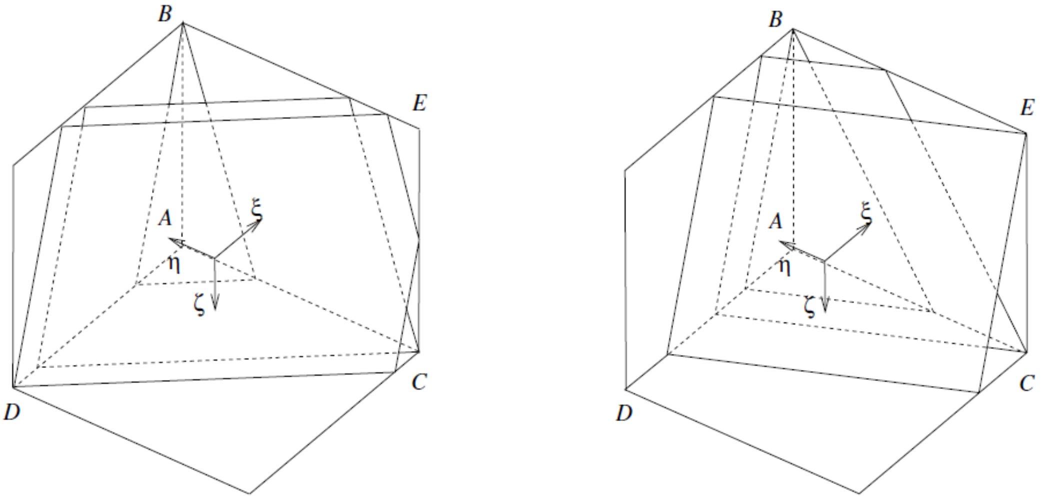

(a) $D_\xi \leq D_\eta + D_\zeta$ (b) $D_\xi > D_\eta + D_\zeta$

Figure 3.2: Plane topologies for $\Phi_k \leq 0$ [19]

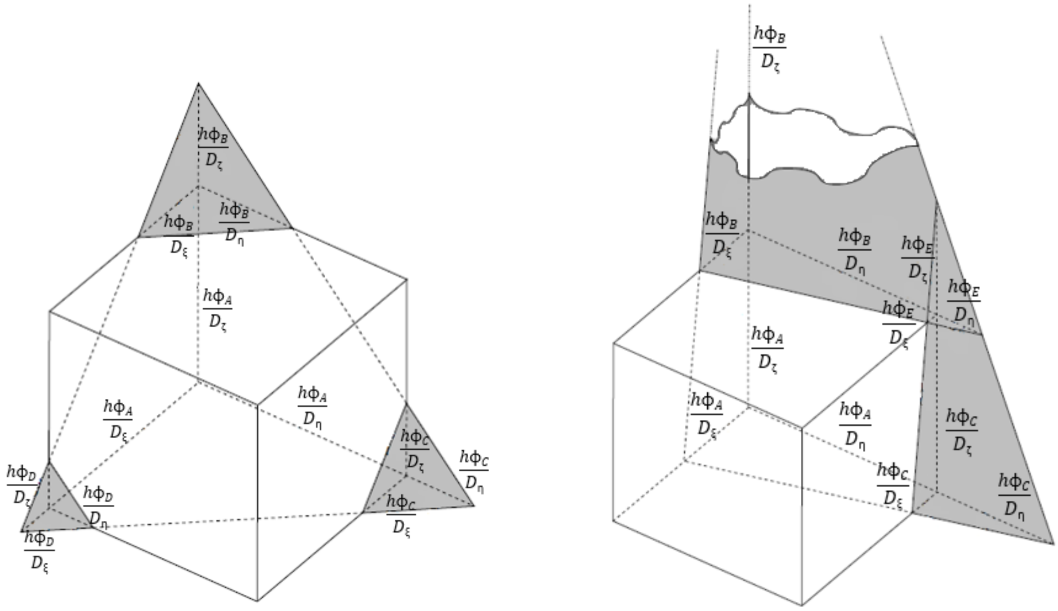

(a) $D_\xi \leq D_\eta + D_\zeta$ (b) $D_\xi > D_\eta + D_\zeta$

Figure 3.3: Area for $\Phi_k \leq 0$. Figure adapted from [19]

$$
\begin{aligned}
Area(cell) = & max(Area(A), 0) - max(Area(B), 0) - max(Area(C), 0) \\
& - max(Area(D), 0) + max(Area(E), 0)
\end{aligned}
\tag{3.10}
$$

Where $Area(B)$ represents the area of the pyramid face which is opposite to the vertex B, this area can be easily calculated using the Heron's formula and from the available information about the sides of the pyramid. These details about the area calculations can be found in Appendix A.

For the limiting conditions where the interfacial plane is parallel to one or two axis, the cell area is given by Eq. 3.11 and Eq. 3.12.

$$\lim_{D_\zeta \to 0} Area(cell) = h^2(\Phi_A - \Phi_C)\sqrt{\frac{1}{D_\xi^2} + \frac{1}{D_\eta^2}} \tag{3.11}$$

$$\lim_{D_\zeta \to 0} \lim_{D_\eta \to 0} Area(cell) = h^2 \tag{3.12}$$

Results of the area calculations

This section covers the result of the interfacial area calculations using the approach followed by Van der Pijl [19]. To validate the results, reference of a spherical geometry was taken. This reference was chosen because:

1. Exact solution is available for the surface area of a sphere.
2. A spherical geometry contains all types of level set values and normal vectors that are expected from other complex geometries.

To get the results, a bubble of unit diameter was initialized in the existing model without gravity and with zero initial velocity everywhere in the domain. Then the area of this bubble was compared to the value of π for different grid sizes. The results are shown in Fig. 3.4. In this figure, D represents the bubble diameter.

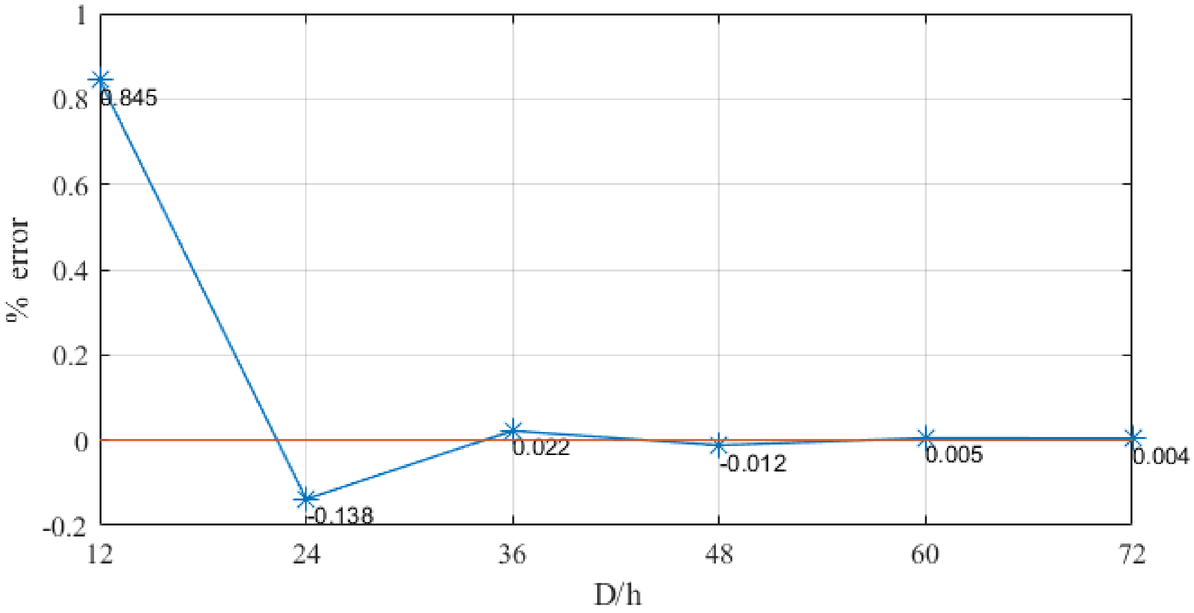

Figure 3.4: Percentage error in area calculation with grid resolution

It is clear from the above figure that the relative error in the area calculations is very less even with a very coarse grid and the solution converges to the exact solution as the mesh resolution is increased. This analysis concludes that this approach can definitely be used to calculate the interfacial area with very high accuracy.

3.2 Nusselt number calculation

The Nusselt number can also be defined as the dimensionless temperature gradient normal to the surface and it is given as,

$$Nu = -\nabla T \cdot \hat{\mathbf{n}} \tag{3.13}$$

Here $\hat{\mathbf{n}}$ is a normal unit vector pointing away from the bubble surface. This normal vector can be calculated by using central difference on the LS function.

$$\hat{\mathbf{n}} = -\frac{\nabla \Phi}{|\nabla \Phi|} \tag{3.14}$$

$$\nabla \Phi_{i,j}(\text{in 2D}) = \left(\frac{\Phi_{i+1,j} - \Phi_{i-1,j}}{2h} \right) \hat{i} + \left(\frac{\Phi_{i,j+1} - \Phi_{i,j-1}}{2h} \right) \hat{j} \tag{3.15}$$

To accurately capture the gradient of temperature at the interface, a quadratic profile was assumed for the temperature variation in the boundary layer. Therefore, ∇T at the surface was calculated using Eq. 3.16.

$$\frac{\partial T}{\partial x} = \frac{T_1 x_2^2 - T_2 x_1^2 + x_1^2 - x_2^2}{x_1 x_2 (x_2 - x_1)} \tag{3.16}$$

The above equation is for only those interfaces which are at $T = 1$. Here T_1 and T_2 are temperatures at x_1 and x_2 positions on the x-axis and $T = 1$ at $x = 0$. The same equation was used for y and z direction temperature gradients. Using Eq. 3.16, gradients in all three directions were calculated for every interfacial cell to obtain the value of the Nusselt number. One of the most critical thing in this method was to identify the position of the origin and to calculate the values of T_1, T_2, x_1 and x_2. The idea was to drop a normal from the centre of the interfacial cell to the interface and the point where this normal intersects the surface was taken as the origin, as shown in Fig. 3.5 .

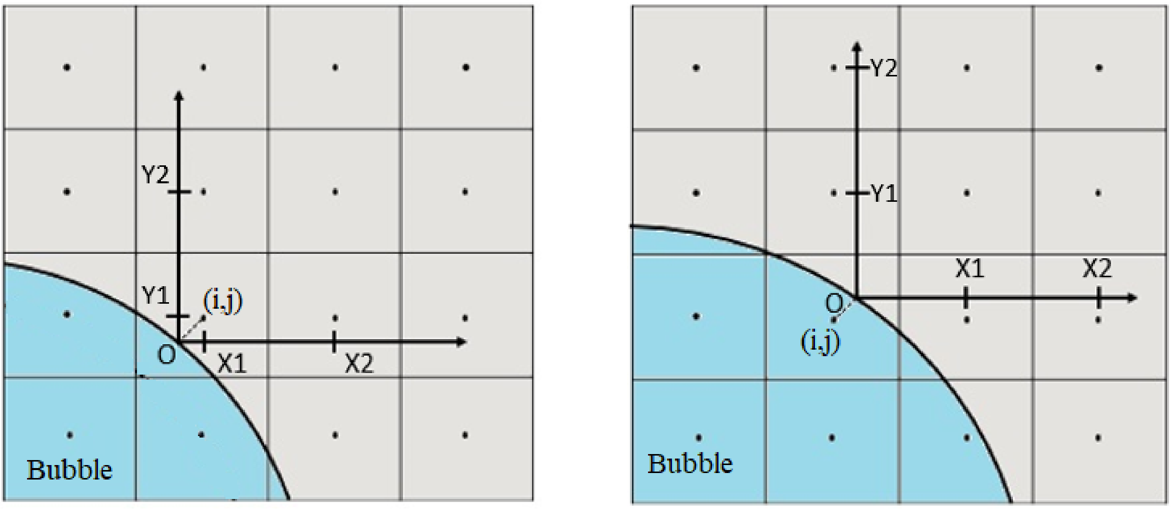

(a) Gradient for $\Phi_{i,j} < 0$ (b) Gradient for $\Phi_{i,j} > 0$

Figure 3.5: Position of the axis for gradient calculations

It is important to note that the new axis may or may not pass through the cell centres. So to calculate the axis temperature at point 1 and 2, the distance average of the adjacent points located at x_1 and x_2 was required.

As an example, to calculate x_1, x_2, T_1 and T_2 for x-axis in Fig.3.5a, the following approach was followed.

$$\begin{aligned}
x_1 &= -\Phi_{i,j}\hat{n}_x \\
x_2 &= x_1 + h \times sign(\hat{n}_x) \\
y_1 &= -\Phi_{i,j}\hat{n}_y \\
T_1 &= \frac{T_{i,j}(h-|y_1|) + T_{i,j-1}|y_1|}{h} \\
T_2 &= \frac{T_{i+1,j}(h-|y_1|) + T_{i+1,j-1}|y_1|}{h}
\end{aligned} \tag{3.17}$$

Where the *sign* function returns 1 when the input is greater than or equal to 0 and -1 otherwise. Similar techniques were applied for the y and z axis and for those interfacial cell points where $\Phi > 0$ (Fig. 3.5b). In 2D geometry, averaging of only two points is required for the temperature calculation at a single point on the axis but in 3D geometry four points were required for the distance averaging. This means that for calculating the temperature gradient in 3D, nine points were required (1 at origin + 4 at x_1 + 4 at x_2) to calculate the gradient in one direction. The distance averaging was not required for those interfacial cell points which were exactly on the interface because for these points, the gradients can be calculated using the adjacent cell centre values.

3.3 Flow geometry and setup

For simulating a bubble rising through a fluid medium different approaches can be followed. One way is to make the computational domain so large that the bubble can achieve it's terminal velocity while moving through the domain. This method can be very inefficient especially when the grid is uniform and stationary. Another method is to keep the bubble stationary by changing the inlet and outlet velocity of the domain as shown in Fig. 3.6. This is almost equivalent to having a frame of reference attached to the bubble considering the assumption that major movement of the bubble will only be in the z direction.

To keep the bubble stationary, the inlet velocity is changed at every time step according to Eq. 3.18, where Z_0 is the initial z co-ordinate of the bubble center at t=0.

$$Velocity_{inlet} = -a(Z_{bubble-center} - Z_0) \tag{3.18}$$

The simulation starts with a stationary bubble at zero inlet velocity with Z_0=5D. As the bubble starts to rise the inlet velocity is increased to a value proportional to the displacement of the bubble from the initial position. The increase in the inlet velocity decelerates the bubble movement and after some time a steady state is achieved where the bubble remains stationary because of the balance of forces.

The value of the constant a was taken as 1000 for this model. The results of this procedure will be discussed in the later sections of this chapter where it is shown that the bubble finally reaches the expected terminal velocity. All the domain sides parallel to the flow direction were with periodic boundary condition. The temperature of the bubble was initialized as T=1 at every time step and the temperature of the incoming fluid was T=0. The validation of this model will be done by comparing the Nu vs θ values of the model with the results of Oellrich et al. [17].

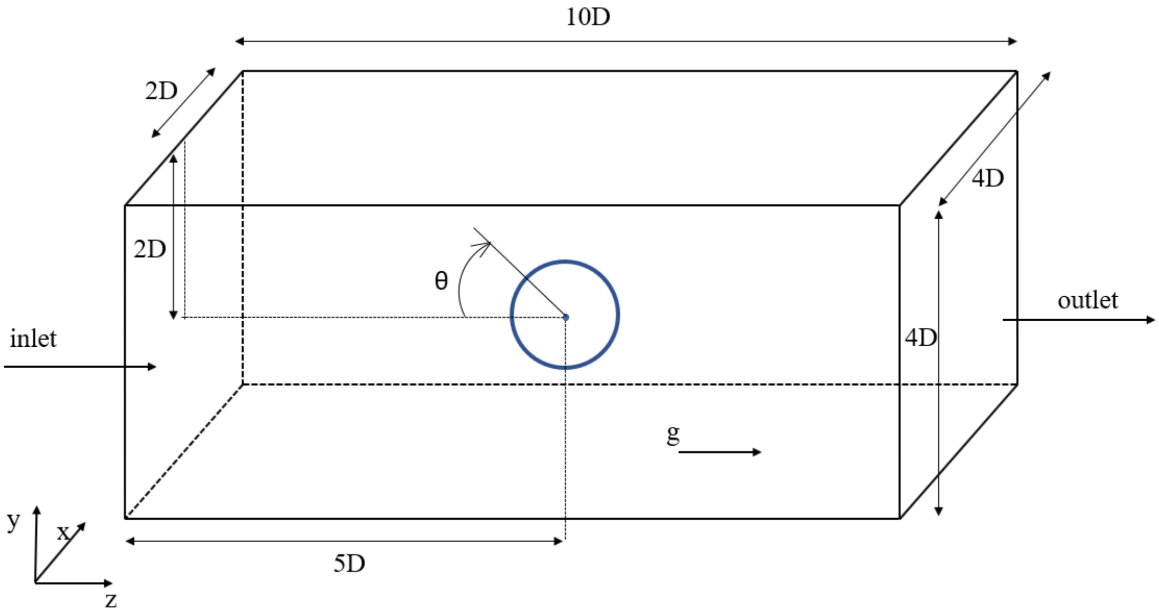

Figure 3.6: Initial configuration of the computation domain setup

3.4 Iteration 1

This iteration is not the final validation of the model but was more intended towards troubleshooting the issues faced during the Nusselt number calculations. Therefore, this section is structured as a root cause analysis to achieve the desired results.

To keep the bubble in the spherical regime of Fig. 3.1. Eotvos number of 0.1 and log(M) number of -10 was chosen, this condition corresponds to an approximate Reynolds number of 80 (from Fig. 3.1). The aim of this section was to compare the results of the model with the information given in Oellrich et. al. [17] for a spherical bubble with Re=80 and Pr=10. The definition of Re and Pr given in Oellrich et. al. [17] were same as the definition considered in this model and are given by Eq. 3.19 and Eq. 3.20. Here u represents the velocity of the bubble.

$$Re = \frac{\rho_c u D}{\mu_c} \tag{3.19}$$

$$Pr = \frac{\mu_c C_{p_c}}{\lambda_c} \tag{3.20}$$

For the conditions given in Oellrich et. al. [17] it was possible to run the model with any thermo-physical property ratio as long as the values of Re and Pr are correct and the bubble remains in the spherical regime with steady state conditions. Therefore, to efficiently run the simulation relatively low values of property ratios were selected. The first iteration was conducted with the fluid properties given in Table 3.1.

Table 3.1: Fluid properties for iteration 1

Property	Bubble	Continuous phase
Density(kg/m^3)	100	202
Viscosity(kg/ms)	1×10^{-4}	2.5×10^{-4}
Surface Tension(N/m)	0.01	
Thermal Conductivity(W/mK)	2.5×10^{-2}	2.5×10^{-3}
Specific Heat(J/kgK)	10	100
Bubble diameter(m)	0.001	
g(m/s^2)	9.81	

Although the above values do not look very realistic but these values were targeted towards the aim of modelling a spherical bubble with Re=80 and Pr=10. These values were chosen so that the system can reach the target values of Eotvos number, Morton number and Prandtl number. The above fluid properties gave the following dimensionless numbers. An important point to note here is that the Reynolds number mentioned in the Table 3.2 doesn't corresponds to the Reynolds number at the terminal velocity, instead it depends on the value of the velocity scale, which can be chosen arbitrarily. In this iteration, the velocity scale was chosen as $\sqrt{gD}$. The real value of the Reynolds number at the terminal velocity can only be found from the simulation results and depends on the physical properties of the fluids. Grid size of D/h=32 was taken for this simulation.

Table 3.2: Dimensionless numbers for iteration 1

Number	
Eotvos number	0.10
Log(M)	-10.02
Reynolds number	80.03
Prandtl number	10

Model results

Finally, the simulation was performed with the above mentioned properties until it reached steady state. Next action was to check,

1. Whether the bubble remains spherical or not.
2. The average value of the Nusselt number over the bubble surface.

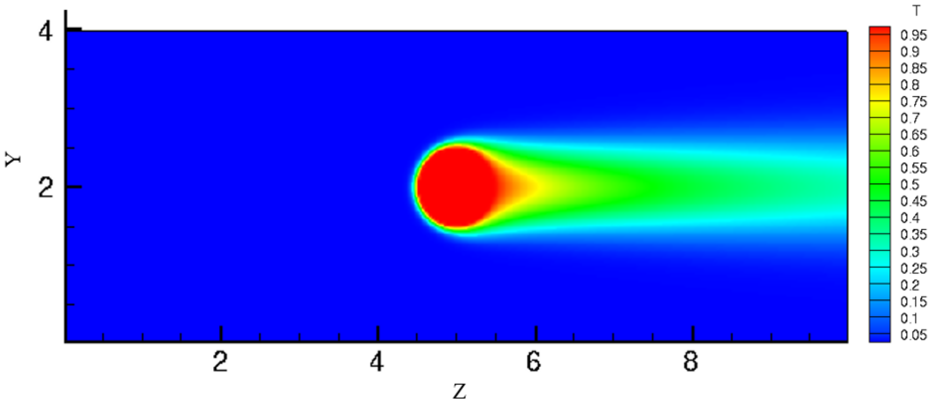

Figure 3.7: Temperature contour for iteration 1

A simple way to check the sphericity of a bubble is to compare it's total area with that of a perfect sphere. Any deviation from the spherical geometry should result in a higher surface area. For this purpose the area of the sphere was divided into 3 parts i.e. for interfacial cell centre points lying outside the interface, inside the interface and on the interface. Although this process was not mandatory to calculate the total area but it gave a good overview of the distribution of the interfacial cell points over the interface.

Table 3.3: Surface area distribution

Interfacial point location	Area
$\Phi > 0$	1.553
$\Phi < 0$	1.586
$\Phi = 0$	0.0102
Total area	3.149
% Deviation from π	0.24%

From the above table it is evident that the deviation from the exact spherical geometry is very less and comparable to the values given in Fig. 3.4. It also shows that the proportion of the area where Φ=0 is very less as compared to Φ <0 or Φ >0. Also the regions of Φ <0 and Φ >0 share almost the same area.

Next step was to compare the average Nusselt number of the model with that of Oellrich et. al. [17]. Since the procedure for calculating the Nusselt number was very complicated because of the large number of data points and also the procedure was slightly different for interfacial points where Φ <0 and Φ >0. So, this analysis was also divided into two regions of Φ <0 and Φ >0.

In Table 3.4, it can be seen that the Nu for Φ >0 is almost comparable to the exact Nu value but for the interfacial points where Φ <0, the procedure gives very unrealistic value of Nu. This much deviation in the average Nusselt number between the interfacial points located at Φ >0 and Φ <0 was neither expected nor acceptable.

The results were checked thoroughly for this anomaly and it was found that this deviation is occurring because of high overestimation of the temperature gradients for

Table 3.4: Nusselt number calculations

Interfacial point location	Nu average
$\Phi > 0$	20.80
$\Phi < 0$	95.44
Exact Nu$_{average}$ [17]	29.93

those points which were located very close to the interface and this overestimation was only occurring for those points which were located outside the interface (Φ <0).

The reason for this issue will be discussed in detail in the next section. From the above results it can only be concluded that the bubble remains in the spherical regime and it is highly likely that the Nusselt number calculations are correct for the points where Φ >0.

Troubleshooting

The reason for high overestimation of the temperature gradients is explained in this section. The method for calculating the slope with quadratic and linear temperature profile is shown in Fig. 3.8. This figure doesn't represent the exact solutions/slopes but it's just a representation of how the solutions would look like on a $T - x$ graph.

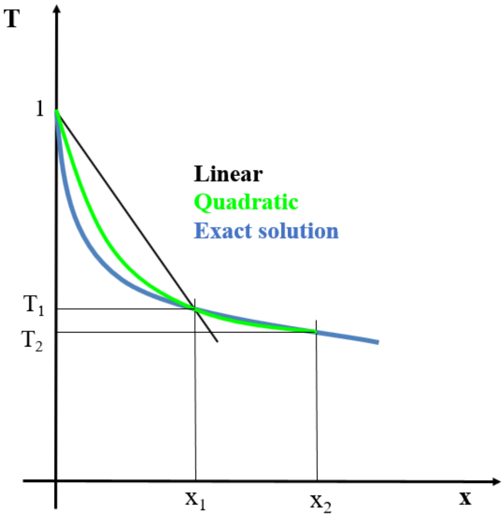

Figure 3.8: Comparison of different slopes

From the figure it is clear that the quadratic slope at $x = 0$ is lesser than the linear slope (but higher in magnitude because the slopes are -ve). It is a very well known phenomenon the linear slope explodes when $x_1 \rightarrow 0$ and from the above graph it is clear that the quadratic slope will always explode earlier than the linear slope when $x_1 \rightarrow 0$. It can also be proven mathematically that $Slope_{quadratic} < Slope_{linear}$ for a typical boundary layer temperature profile.

From the details given in Fig. 3.8, the quadratic and linear slope at $x = 0$ can be given as,

$$Slope_{quadratic} = \left(\frac{\partial T}{\partial x}\right)_{x=0} = \frac{T_1 x_2^2 - T_2 x_1^2 + x_1^2 - x_2^2}{x_1 x_2 (x_1 - x_2)} \tag{3.21}$$

$$Slope_{linear} = \left(\frac{\partial T}{\partial x}\right)_{x=0} = \frac{T_1 - 1}{x_1} \tag{3.22}$$

From the above relations it can be proved that $Slope_{quadratic} < Slope_{linear}$ is always true when,

$$\left(\frac{T_1 - 1}{x_1}\right) < \left(\frac{T_2 - 1}{x_2}\right)$$

which is true for a typical temperature boundary layer profile. Therefore, the above analysis proves that it is always better to use linear slope instead of a quadratic slope where $x_1 \rightarrow 0$.

Fig. 3.9 shows the comparison of the average Nusselt number calculated using the linear and quadratic slopes from the model results. It covers only those interfacial points where Φ <0. The x-axis in this graph represents the area loss which is because of the elimination of those interfacial cells centres which are very close to the interface. Therefore a higher area loss represents that a higher number of interface cells were eliminated from the calculations. It is clear from Fig. 3.9 that the linear method of slope calculation is better for those points where $\Phi < 0$ and it shows good results with less area loss.

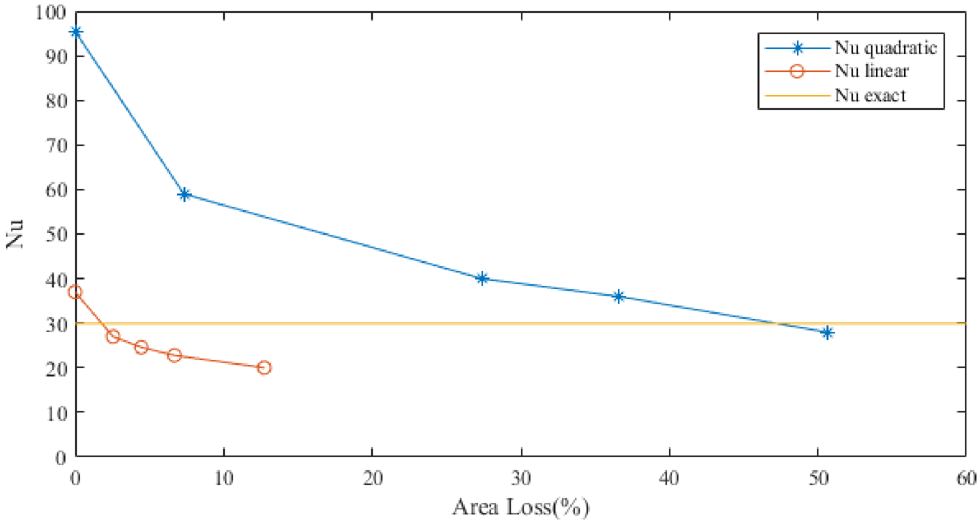

Figure 3.9: Nu comparison through quadratic and linear method for $\Phi < 0$

Although an area loss of 0% is the most desirable condition for the Nusselt number calculations, but from Fig. 3.9 it can be proven that even the linear slope is overestimating the Nusselt number at zero area loss. Therefore, some area loss in the Nusselt number calculations is unavoidable. However, this area loss shouldn't significantly affect the results of the Nusselt number distribution or the average Nusselt number as long as the total area loss is restricted to lower values because there is no preferential elimination of area from some direction and these eliminated interfacial cells are randomly located over the bubble surface area.

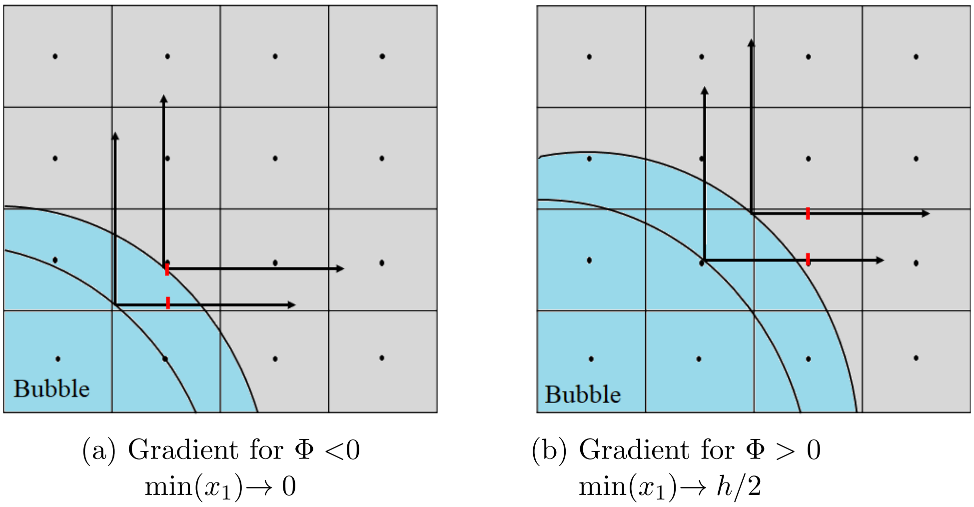

(a) Gradient for $\Phi < 0$
$\min(x_1) \rightarrow 0$

(b) Gradient for $\Phi > 0$
$\min(x_1) \rightarrow h/2$

Figure 3.10: Gradient calculation for different level sets. x_1 represented by red markings.

After all this analysis, it is clear that it is better to calculate the Nusselt number using linear slopes for the points where $\Phi < 0$ because a quadratic slope will explode much earlier than a linear slope as $x_1 \rightarrow 0$. However, this overestimation of Nu was not observed for the points where $\Phi > 0$ as given in Table 3.4. The reason for this anomaly can be explained from Fig. 3.10. This figure shows the positions of the interface for which x_1 acquires it's maximum and minimum values. From this figure it is clear that x_1 can approach to a minimum value of zero for $\Phi < 0$ but for $\Phi > 0$ it can only go to a minimum value of $h/2$. This difference is the reason for Nu overestimation only for those points where $\Phi > 0$.

It is also possible to use linear slope for the points where $\Phi > 0$ but further analysis shows that if the quadratic slope is replaced by the linear slope for these points then the outcome is highly underestimated value for the Nusselt number(≈ 14). Therefore, it can be concluded that to achieve the best results without high grid refinement, a hybrid approach should be adopted where the linear slopes should be used where $\Phi < 0$ and quadratic slope where $\Phi > 0$. Fig. 3.11 shows the result of using the hybrid approach and compares the results with the exact solution of Nusselt number distribution over the bubble surface from Oellrich et. al. [17].

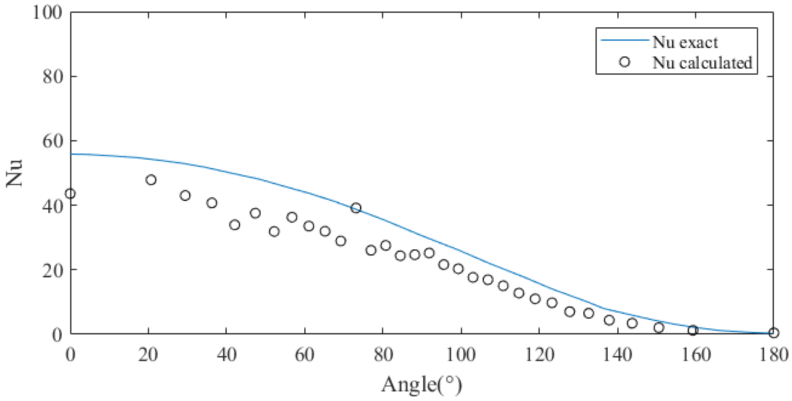

Figure 3.11: Comparison of the calculated Nusselt number with the exact solution

From Fig. 3.11 it is clear that the method has high inaccuracies in the values and the error increases at low angles. The main reason for high error at low angles is because the grid is unable to resolve the boundary layer properly at the front face of the bubble. The high fluctuations in the value can be attributed to some overestimated values of the linear slope. The Fig. 3.11 contains values with zero area loss, so any reduction in error with higher area loss was not possible. Therefore, it was decided to run the next simulation with Pr=1 instead of Pr=10 to resolve the boundary layer effectively. Moreover, it was observed that the real Reynolds number achieved in the simulation was around 92 instead of the target value of 80. So the real error of the model should be higher than the error observed in Fig. 3.11.

3.5 Final Results

After the analysis made in iteration 1, the following changes were made in the model.

1. Fluid properties were changed to run the model at Pr=1, so that the boundary layer can be captured more accurately.

2. Fluid properties were slightly tweaked to get higher Morton number. This was done to achieve steady state Reynolds number close to 80.

The results of the model were compared with the case of Re=80 and Pr=1 from Oellrich et al. [17]. The following fluid properties and dimensionless numbers were used in this model to achieve Pr=1, Re=80 with a spherical bubble.

Table 3.5: Fluid properties used in the final iteration

Property	Bubble	Continuous phase
Density(kg/m^3)	100	202
Viscosity(kg/ms)	1×10^{-4}	2.7×10^{-4}
Surface Tension(N/m)	0.01	
Thermal Conductivity(W/mK)	0.25	0.025
Specific Heat(J/kgK)	10	92.6
Bubble diameter(m)	0.001	
g(m/s^2)	9.81	

Table 3.6: Dimensionless numbers for the final iteration

Dimensionless number	
Eotvos number	0.10
Log(M)	–9.88
Reynolds number	74.1
Prandtl number	1

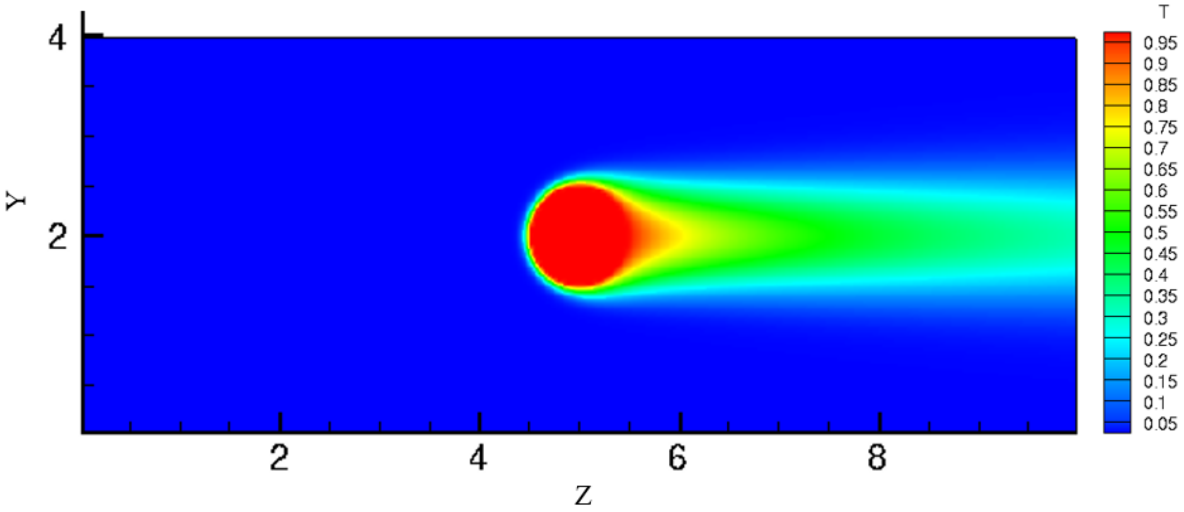

Figure 3.12: Temperature contour for Pr=1 and Re=81.4

Fig. 3.12 shows the temperature contour of the domain and Fig. 3.13 gives the evolution of the Reynolds number and average temperature of the continuous phase. This ensures that the system has reached it's thermal and hydrodynamic steady state. From Fig. 3.13 it can be seen that the steady state Reynolds number is about 81.4, which is close enough from our target value of 80 and it ensures that the Nusselt number comparisons can be made more accurately. It was also observed that the deviation in the surface area from a perfect spherical geometry was only 0.27%, which is a reasonable value to continue for the next step of Nusselt number calculations.

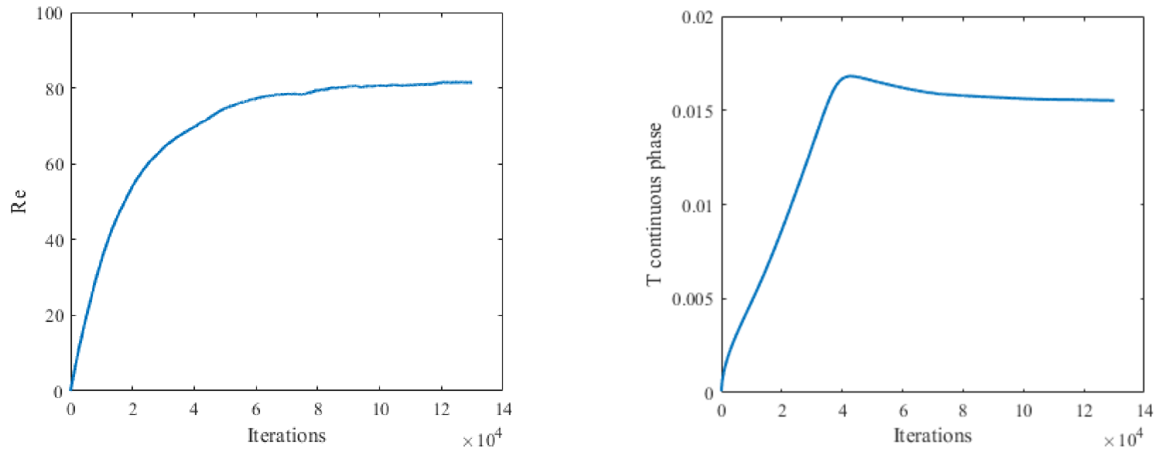

(a) Re evolution

(b) Temperature evolution

Figure 3.13: Evolution of Reynolds number and average temperature of continuous phase

The bump in Fig. 3.13b at about 40,000 iterations should be because of the evolving velocity field. The effect of changing the Prandtl number is evident by comparing the Fig. 3.12 and Fig. 3.7, higher Prandtl number gives thinner temperature streak at the trailing side of the bubble which is due to lower heat diffusion. The effect of changing the Prandtl number on the thickness of the boundary layer is more evident from Fig. 3.14. It is clear that now the temperature boundary layer cover more numbers of grid cells, hence it was expected to get more accurate results for the Nusselt number calculations.

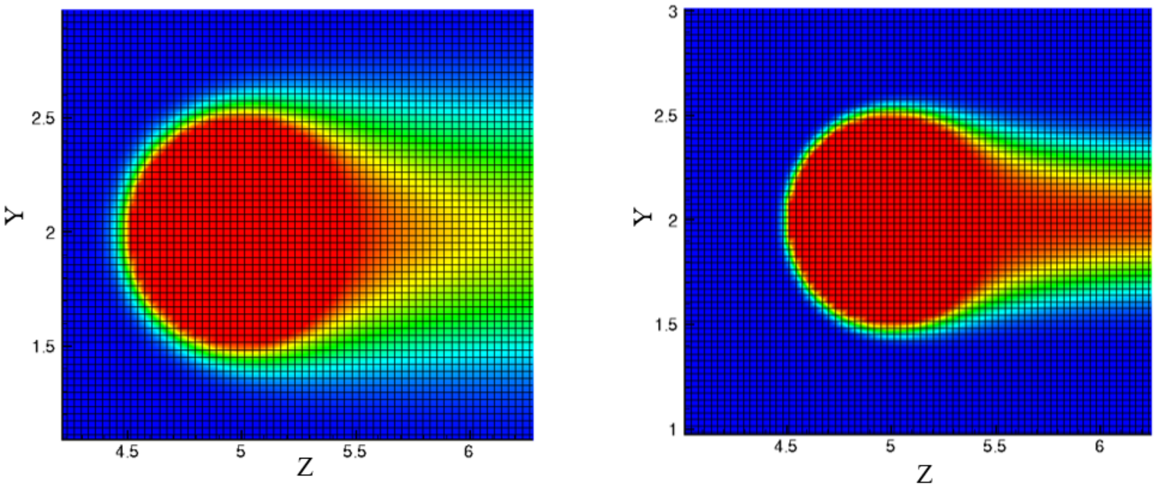

(a) Boundary layer for Pr=1 (b) Boundary layer for Pr=10

Figure 3.14: Boundary layer thickness for different Prandtl numbers

Nusselt number calculations

For the calculation of the Nusselt number, the hybrid approach developed in the last section was used. Table 3.7 compares the exact value of the average Nusselt number from Oellrich et. al. [17] with the values calculated from this model at steady state. The calculated values are for two different types of conditions depending upon the number of interfacial points which were excluded from the calculations. The calculations show a very good agreement with the exact values of the Nusselt number.

Table 3.7: Average Nusselt number comparison

	Nusselt number	Area loss	Excluded points
Nu_{exact} [17]	10.55	–	–
Nu_{avg}	10.68	11.83%	$-h/10 < \Phi < 0$
Nu_{avg}	11.57	1.64%	$-h/50 < \Phi < 0$

To check the accuracy of both the linear and quadratic slopes, a comparison was required for these individual methods with the exact Nusselt number values. Table 3.8 gives the values of Nu for this analysis. It is clear from this data that the linear slope slightly underestimates the exact value and the quadratic slope slightly overestimates the value of the Nusselt number. This analysis makes it clear that the Nusselt number calculations are correct and both quadratic and linear slopes are approaching the same value.

After ensuring that the average Nusselt number is correct, it is important to check the distribution of the Nusselt number over the surface of the bubble and compare it

Table 3.8: Nusselt number comparison for inside and outside interfacial points for 11.83% area loss case

Nusselt number distribution	
Nu_{avg} at $\Phi > 0$	10.92
Nu_{avg} at $\Phi < 0$	10.33

with the reference of Oellrich et. al. [17] for Re=80 and Pr=1. Fig. 3.15 shows this distribution starting from the facing side of the bubble to the trailing side. This figure makes it clear that after excluding more interfacial points which are closer to the interface, the fluctuations in the Nusselt number decreases and it ensures a smoother distribution.

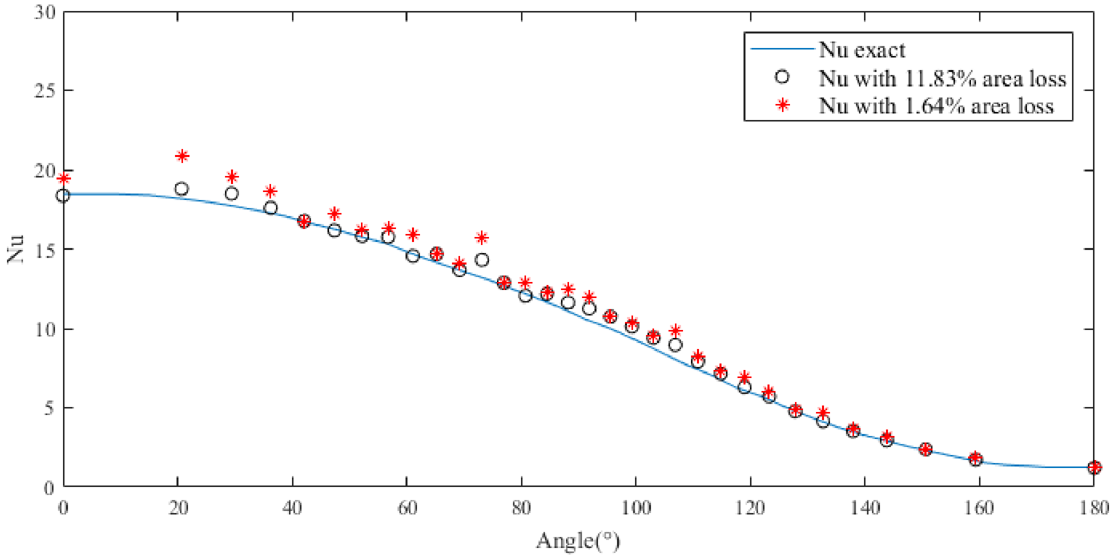

Figure 3.15: Comparison of Nusselt number distribution over the bubble surface

All the analysis done in this section concludes that the Nusselt number distribution over the bubble surface is in a very good agreement with the solution given by Oellrich et. al. [17] and it concludes that the heat transfer model is working perfectly. This means that this model can be used further for analyzing more complicated heat transfer behaviour in multiphase flows.

At last, the average value of the Nusselt number can also be compared to the value of the global Nusselt number obtained from the energy balance of the bubble. This procedure is given in Appendix C and it gives an average Nusselt number of 8.86 for the final results, which is an underestimation from the exact values. This underestimation could be because of the error in estimating the temperature of the interfacial cells and it can be reduced by adopting a finer grid.

4 Heat transfer in coalescing droplets

This chapter covers the study of heat transfer between two coalescing droplets and the surrounding fluid. This case is same as the case covered by Kwakkel [3] for head on collision between two tetradecane droplets in air with Weber number(We)=2.3 but now it is with the addition of a heat transfer model. To analyze the heat transfer in this chapter, first a new method of Nusselt number calculation is derived and after that this method is used to analyze the heat transfer in two coalescing tetradecane droplets.

4.1 Nusselt number calculation

The approach for calculating the Nusselt number developed in Chapter 3 gave reasonably accurate results for completing the model validation. However, in most of the heat transfer analysis the interface temperature is not known. Therefore to calculate the Nusselt number at the interface, it is important to calculate the interface temperature first.

The interface temperature is obtained by a heat flux balance between two points on the either side of the interface i.e. if the interfacial cell point is inside the interface, then it is required to chose another close by point outside the interface for the energy balance. For easy representation, a 2D geometry is used in this explanation. The choice for the second point is made using Eq. 4.1.

$$\begin{aligned} i_2 &= i_1 + sign(\hat{n}_x) \\ j_2 &= j_1 + sign(\hat{n}_y) \end{aligned} \tag{4.1}$$

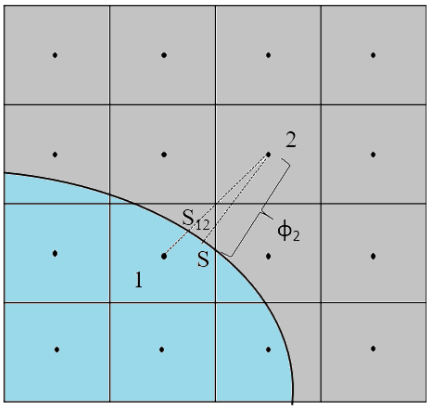

Figure 4.1: Heat balance for Nu calculations

Balancing heat flux along the direction of line 1-2 in Fig. 4.1 gives,

$$\lambda_d\left(\frac{T_{S_{12}}-T_1}{|\Phi_1|}\right)=\lambda_c\left(\frac{T_2-T_{S_{12}}}{|\Phi_2|}\right) \tag{4.2}$$

From the above equation, the surface temperature at the surface S_{12}, between point 1 and 2 can be calculated. Now for calculating the Nusselt number at the interface, it is assumed that the point S (this is obtained after dropping a perpendicular from point 2 to the interface) and S_{12} have the same temperature. The accuracy of this assumption should increase with more refined computational grids. Therefore, the Nusselt number at the surface can be calculated by,

$$\begin{aligned} Nu &= -\frac{\partial T}{\partial \eta}=\frac{T_s-T_2}{|\Phi_2|} \\ &= \frac{\lambda_d(T_1-T_2)}{\lambda_d|\Phi_2|+\lambda_c|\Phi_1|} \end{aligned} \tag{4.3}$$

The above relation for calculating the Nusselt number uses linear slopes for estimating the temperature gradients. Therefore, it's not expected from this relation to give very accurate results but at the same time it has one advantage over the linear slope method of Chapter 3. This advantage is that it is possible to evaluate the Nusselt number over the complete surface area because the denominator in Eq. 4.3 doesn't tends to zero even if the interfacial points are very close to the interface.

4.2 Test case for checking Nusselt number calculations

This section is dedicated to check the applicability of the Nusselt number calculation method explained in the last section. For this purpose, a rising bubble was simulated with the same computational setup as given in the last chapter (see Fig. 3.6) with the exception that the temperature of the bubble was initialized only for the first time step, this was done to ensure that there is a variable temperature field inside the bubble as well. The properties used for this simulation and the corresponding dimensionless numbers are given in Table 4.1 and Table 4.2.

Table 4.1: Fluid properties for test case

Property	Bubble	Continuous phase
Density(kg/m^3)	10	400
Viscosity(kg/ms)	1×10^{-4}	2.5×10^{-4}
Surface Tension(N/m)	0.01	
Thermal Conductivity(W/mK)	0.25	0.025
Specific Heat(J/kgK)	2.5×10^{3}	100
Bubble diameter(m)	10^{-3}	
g(m/s^2)	9.81	

Table 4.2: Dimensionless numbers for the test case

Number	
Eotvos number	0.383
Log(M)	-10.03
Reynolds number	158.47
Prandtl number	1

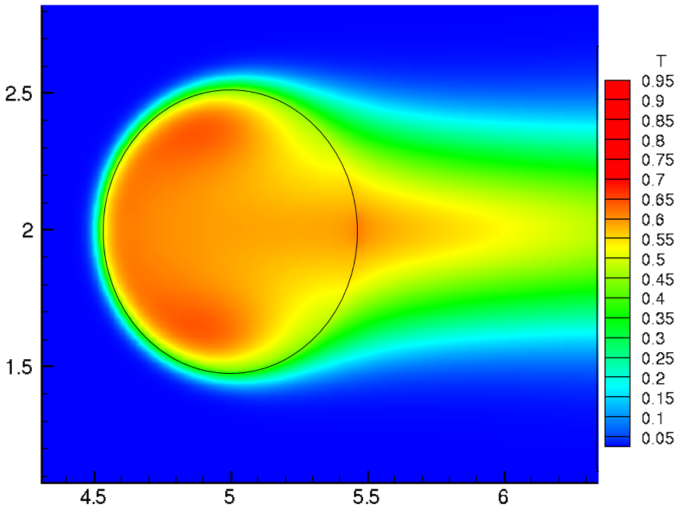

Figure 4.2: Temperature field of the test case. Interface is represented by a black curve.

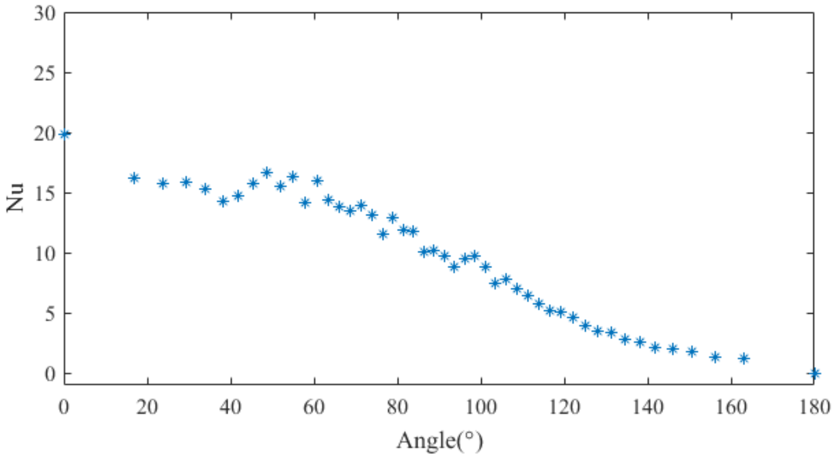

Figure 4.3: Nusselt number distribution for the test case

The main aim behind this analysis is to check the reliability of the Nusselt number calculations. Therefore, the grid resolution of this simulation was kept at $D/h = 50$. Fig. 4.2 shows the temperature field of the bubble and surrounding fluid after 30,000 iterations. The interface is represented by a black curve. Fig. 4.3 show the distribution of Nusselt number over the bubble surface. The trend of the Nusselt number distribution is almost similar to that of a bubble with constant temperature, which was covered in the last chapter. However, there are two main differences. Firstly, there is a slight bump in the

Nusselt number profile at about 50°-70° angle. This bump can be attributed to the high temperature region occurring at about the same angle in the bubble as seen in Fig. 4.2. Another minor difference is that the Nusselt number calculated at 180° gives a negative value. The reason for this negative value is the high temperature region occurring just outside the bubble interface at the trailing surface of the bubble, this can also be observed in Fig. 4.2. The above analysis proves that the new Nusselt number calculations are good enough to qualitatively understand the heat transfer distribution in multiphase flow and of course, the accuracy of these calculations should increase with the grid refinement.

4.3 Case of coalescing droplets

In this section, the Nusselt number calculation method of the last section is used to analyze the phenomenon of heat transfer in coalescing droplets. The physical properties of the fluid and film drainage time are same as the one covered by Kwakkel [3] for tetradecane droplets in air for We=2.3.

Computational domain setup

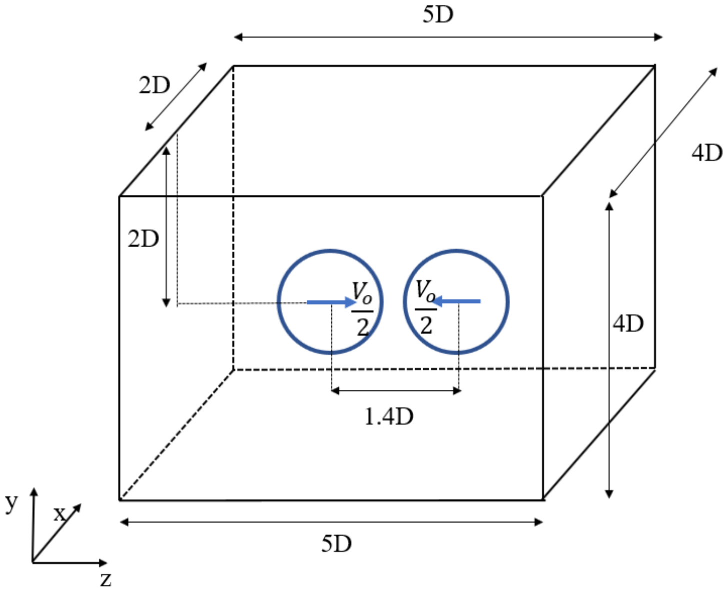

Figure 4.4: Computational domain setup for droplets coalescence

The computational domain setup is shown in Fig. 4.4. Here, two tetradecane droplets are initialized with $V_o/2$ velocities towards each other in the z-direction, where V_o=0.61 m/s is the characteristic velocity scale of the model. The two droplets coalesce when the contact time between the two droplets exceeds the film drainage time of this model. This film drainage time was determined experimentally from the results of Pan et al. [20] and is given in Table. 4.3. Boundary conditions for velocities and temperature were symmetric at y-z and x-z plane and periodic for x-y plane boundaries. Pressure was kept zero at the y-z and x-z plane boundaries and periodic for x-y plane. D/h was kept equal to 24 for this simulation.

Table 4.3: Fluid properties for coalescing droplets

Property	Tetradecane droplets	Air
Density(kg/m^3)	762	1.225
Viscosity(kg/ms)	2.128×10^{-3}	1.827×10^{-5}
Surface Tension(N/m)	2.65×10^{-2}	
Thermal Conductivity(W/mK)	0.139	2.624×10^{-2}
Specific Heat(J/kgK)	2.214×10^{3}	1.005×10^{3}
Droplet radius(m)	$1.072\times\ 10^{-4}$	
Film drainage time(ms)	0.270	

Results of the model

This section discusses the evolution of the Nusselt number over the droplet interface before, during and after coalescence. Fig. 4.5 shows the temperature contour and interface position of the model at t=0. The interface position is tracked using the level set function. All the displayed sections mentioned in the results are for a $y-z$ plane passing through $x = 2D$. The irregularities observed in the temperature field is because of the coarseness of the grid. However, these irregularities are only observed for the first few iterations because after some steps the temperature field diffuses to make the gradients less sharp. In the next few pages, the evolution of the Nusselt number at the droplet interface is discussed. This Nusselt number is calculated by averaging all the Nusselt numbers for a particular xy-plane. Therefore, the Nusselt number is plotted with respect to z direction. To easily compare the Nusselt number values, the scale of the axis is kept same for all the figures. As observed in Fig. 4.6, the evolution of the Nusselt number is as expected. The droplets show higher Nusselt numbers before the collision than during or after the collision, this should be because of the decrease in velocities of the droplets after the collision. Ideally, the symmetry plane passing through the $z = 5D/2$ should show zero value for the Nusselt number during the time when the droplets are touching each other but because of the coarseness of the grid, this absolute zero value is difficult to capture. However, from the Nu figures it is clear that the Nusselt number at this symmetry plane is much lower than other regions. One more important thing to note is that after the coalescence is complete, the Nusselt number profile gradually becomes more uniform.

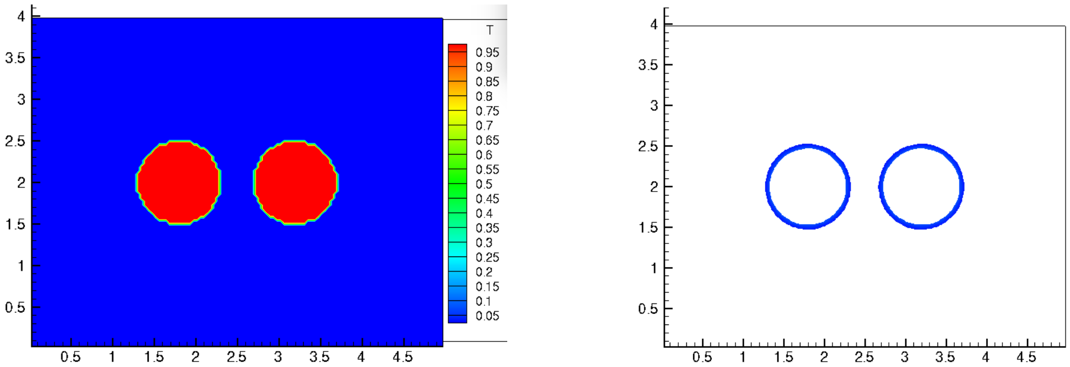

(a) Temperature field at t=0

(b) Interface position at t=0

Figure 4.5: Initial conditions

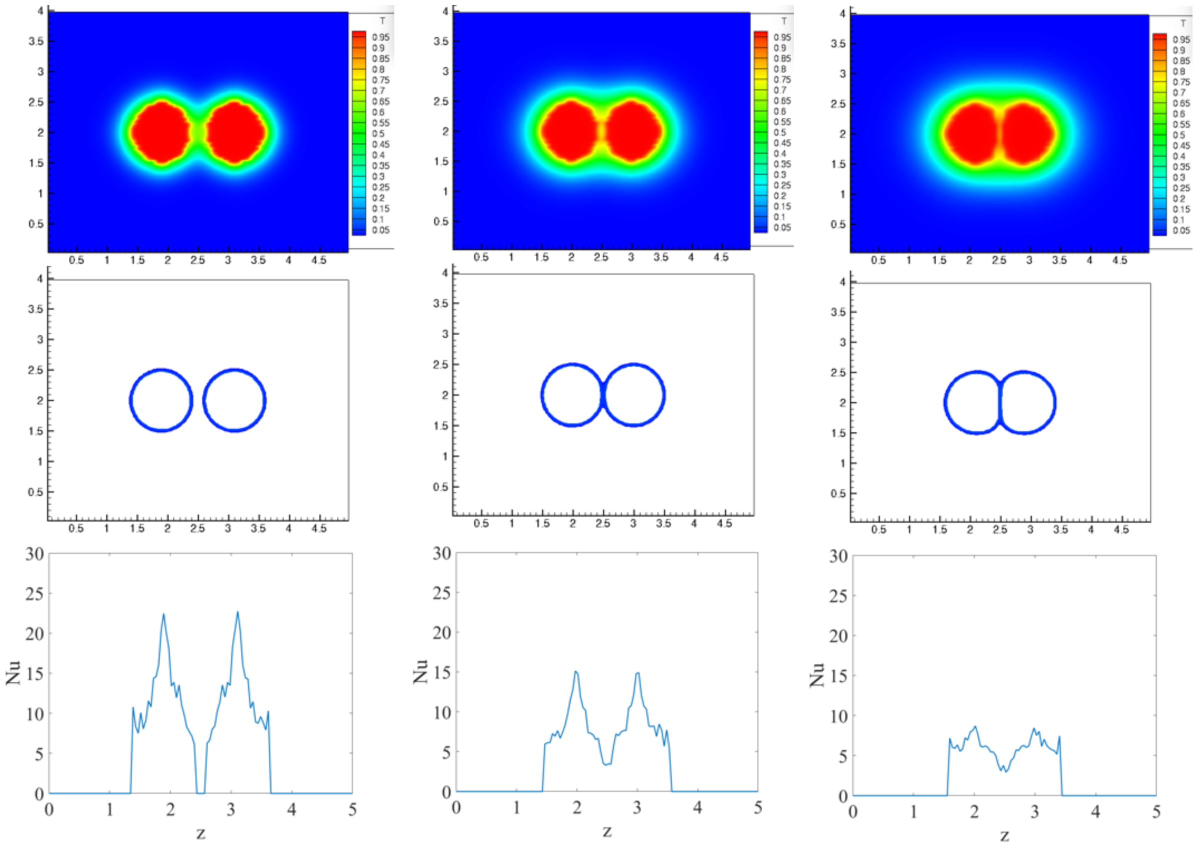

(a) t=0.070 ms (b) t=0.140 ms (c) t=0.211 ms

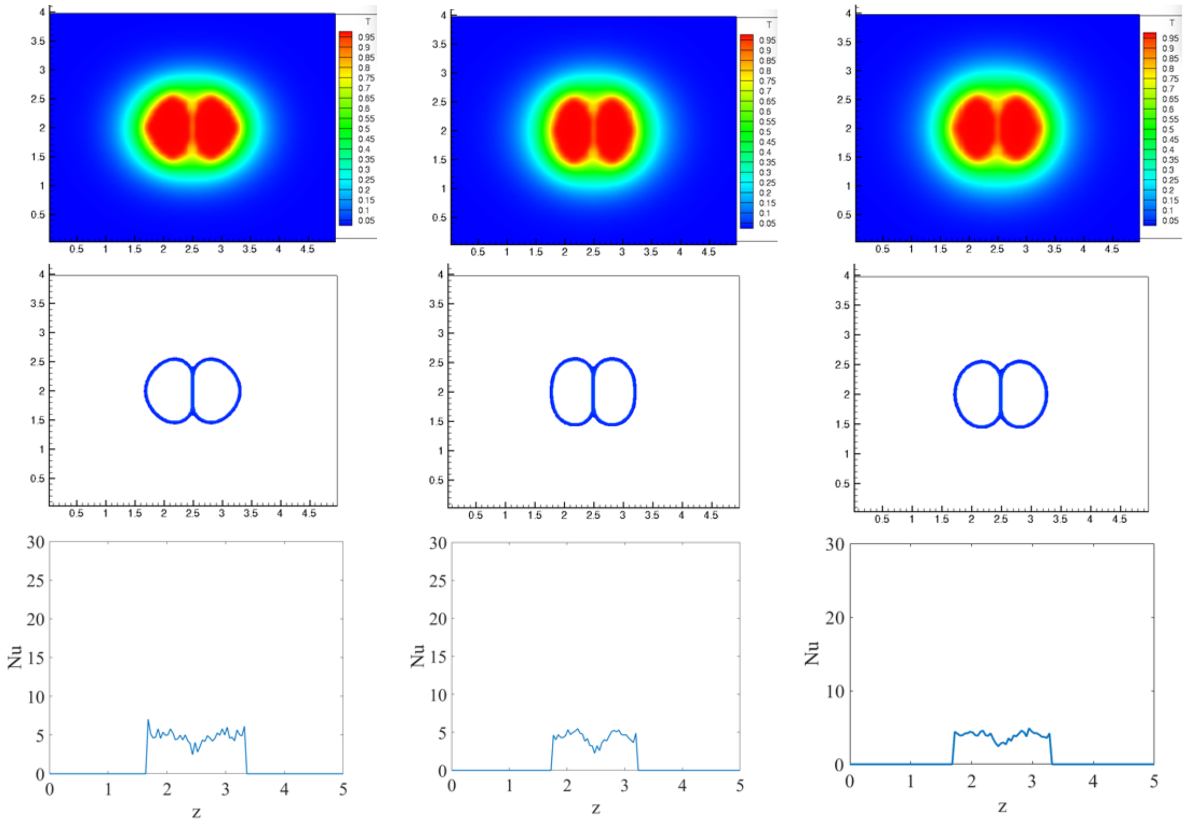

(d) t=0.281 ms (e) t=0.351 ms (f) t=0.422 ms

Figure 4.6: Temperature field, interface and Nusselt number evolution

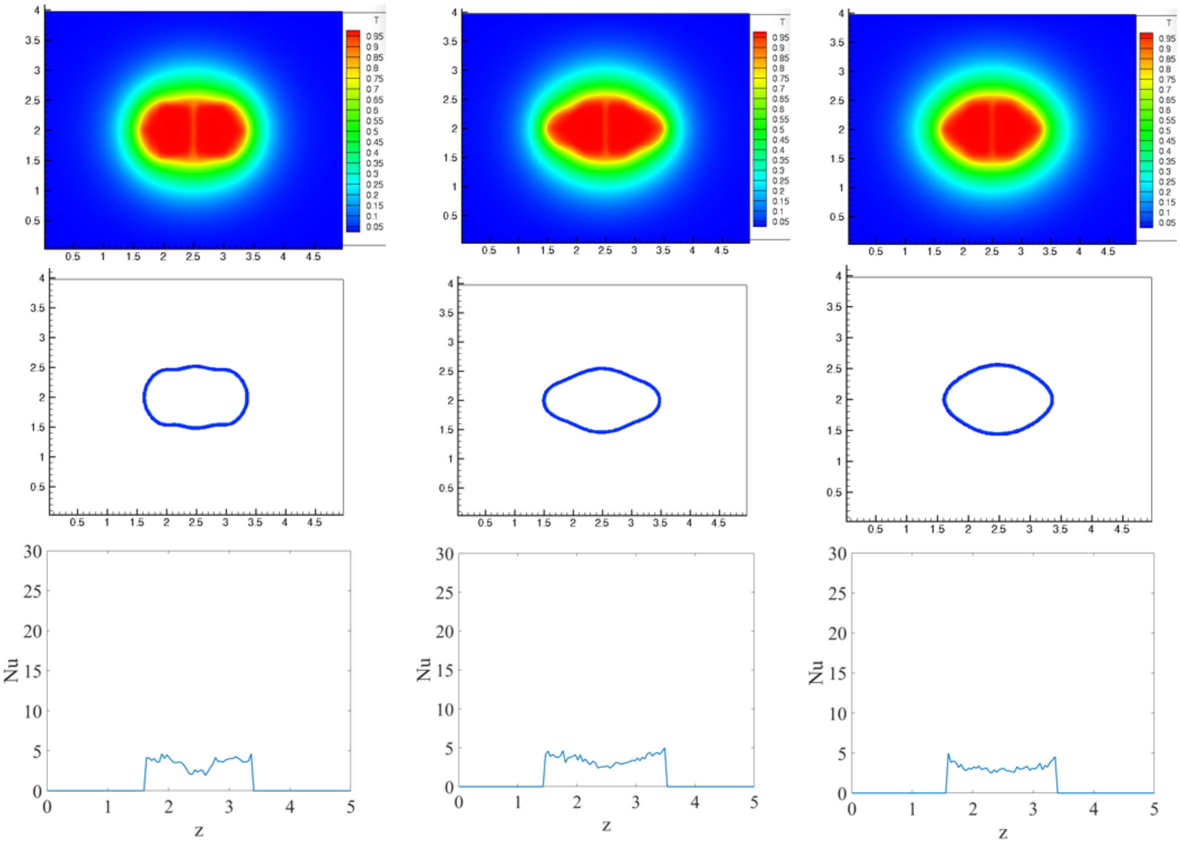

(g) t=0.492 ms (h) t=0.562 ms (i) t=0.633 ms

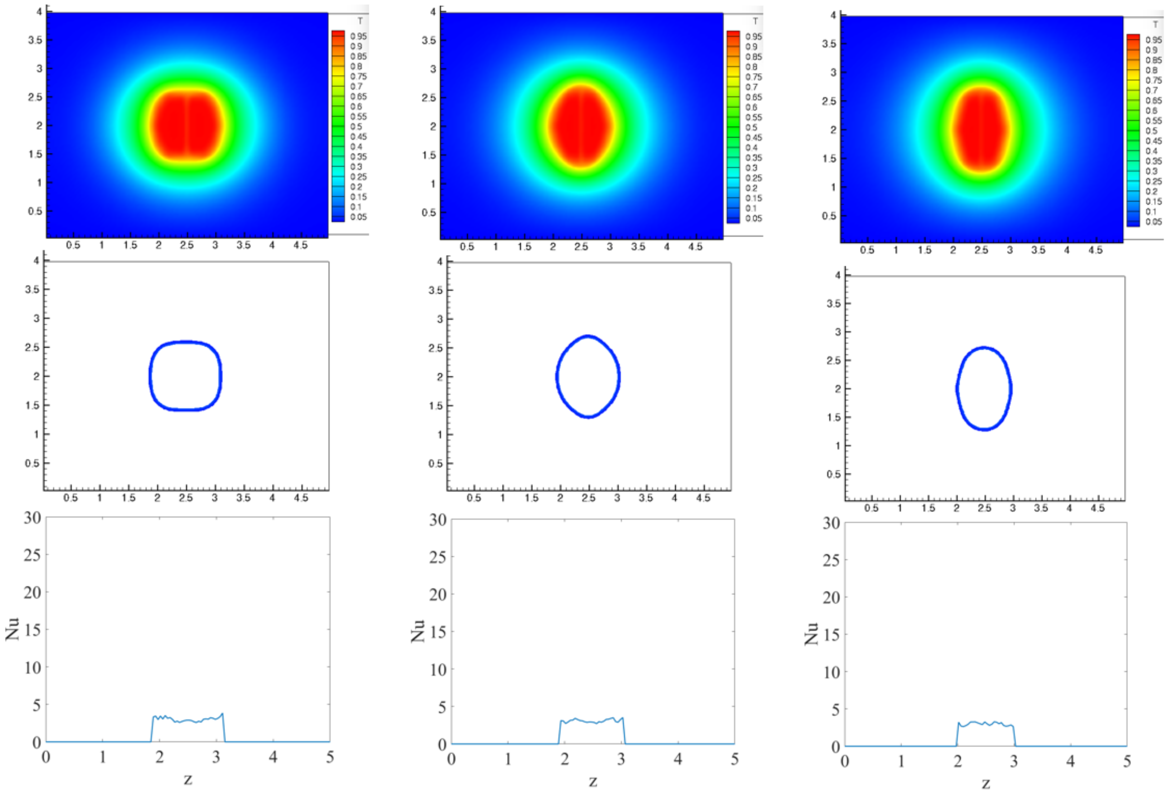

(j) t=0.703 ms (k) t=0.773 ms (l) t=0.843 ms

Figure 4.6: Temperature field, interface and Nusselt number evolution

Surface area evolution

Fig. 4.7 describes the evolution of the total surface area in this simulation. It also shows the number of droplets/interfaces in the simulation. From this figure it can be inferred that the coalescence takes place between 0.4 ms to 0.5 ms because the number of droplets decreases from 2 to 1 during this time period. The area calculation is done considering that the initial droplet diameter is 1 units. This figure also shows the minimum limit of the interfacial surface area for a particular number of interfaces based on the fact that a spherical geometry has the minimum surface area for a fixed volume. Therefore, the calculated surface area should be greater than or equal to this area limit. The area evolution trend is as per the expectations, with a sharp drop between t=0.4 ms and t=0.5 ms. However, the area calculations for the cases around t=0.4 ms shows an anomaly. The area calculated in this time zone is slightly lower than the minimum limit for 2 droplets. Due to time limitations, it was not possible to exactly find the root cause of this issue. However, it is still possible to use this area calculations for heat transfer analysis because these calculations are good enough to capture the trend of area evolution with acceptable errors.

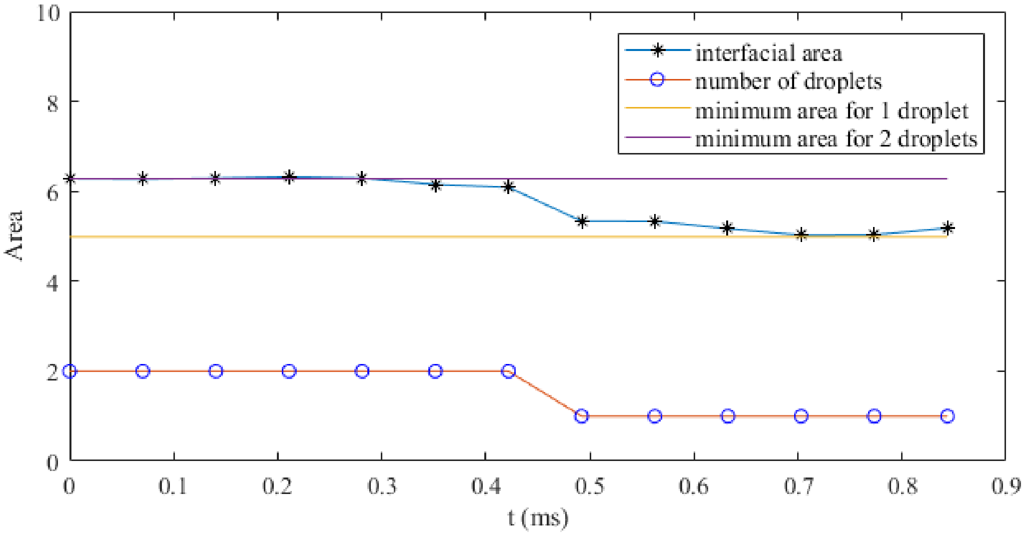

Figure 4.7: Area evolution with time for droplets coalescence

4.4 Conclusion

The Nusselt number calculation method developed in this chapter is able to capture the trend of heat transfer in both the cases. Therefore, it can be further used to analyze heat transfer in other cases too. The area calculations are also able to capture the trend of the interfacial area evolution in the case of coalescing droplets. The validation of the heat transfer model and the analysis done in this chapter concludes that this model can definitely be used to capture the interfacial heat transfer in multiphase flows for a variety of flow configurations with very good accuracy.

5 Conclusions and recommendations for future work

This chapter is dedicated to summarize the conclusions made in this thesis and to propose some future work to improve the existing model. All these remarks are given below,

1. The method of interfacial area calculation shows a very good agreement with the exact solution. However, there are some minor anomalies observed in the droplets coalescence case, which should be further investigated.
2. A hybrid method of local Nusselt number calculation was developed during the process of model validation, which enabled to accurately capture the Nusselt number at the interface without very high grid refinement.
3. The heat transfer model has been thoroughly validated using the available literature. This ensures that the model is working perfectly and can be used for the analysis of heat transfer in other complex cases.
4. A method to calculate the global Nusselt number was also proposed. It is important to further explore the possibility of using this method. For this, it is vital to do a convergence analysis of the Nusselt number calculations through the global energy balance and through the averaging of local Nusselt number at the interface.
5. The analysis performed for the heat transfer between coalescing drops and surrounding air shows an expected behaviour of the Nusselt number variation over the computational domain at different time steps.
6. A new method of Nusselt number calculation was used in Chapter 4, which might not be as accurate as the hybrid approach developed earlier but it definitely gives good qualitative results. It is recommended to combine the hybrid approach and the new method to capture the local Nusselt number accurately.
7. Furthermore, to increase the applicability of this model, the possibility of including a phase change model to capture evaporation/condensation phenomena should be explored.

Appendix A: Surface area calculations

This section include the details about calculating the interfacial area in a computational cell for use in Eq. 3.10. To keep things brief, only $area(A)$ of Eq. 3.10 is calculated here. The only change for calculating the base area of other pyramids is to change the corresponding level set value. $area(A)$ can be calculated by calculating the area of the shaded face in Fig. .1.

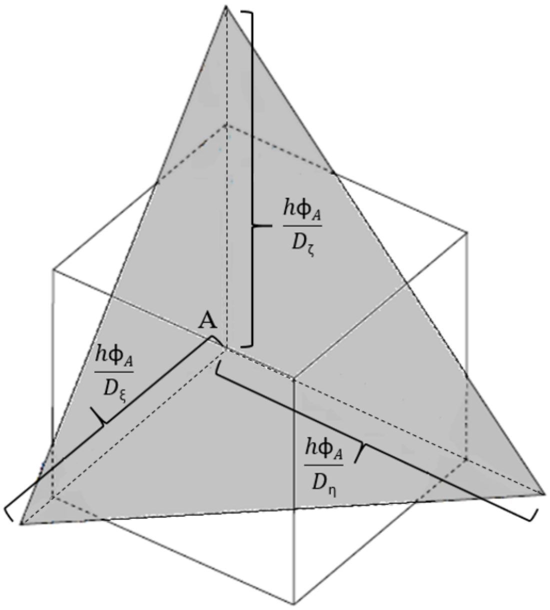

Figure .1: Calculation of interfacial area

The sides of this shaded face can be given as,

$$s_1 = h\Phi_A\sqrt{\frac{1}{D_\xi^2}+\frac{1}{D_\eta^2}} \qquad s_2 = h\Phi_A\sqrt{\frac{1}{D_\xi^2}+\frac{1}{D_\zeta^2}} \qquad s_3 = h\Phi_A\sqrt{\frac{1}{D_\eta^2}+\frac{1}{D_\zeta^2}}$$

Now using Heron's formula, the area of the face can be calculated using the following equations.

$$s = \frac{s_1+s_2+s_3}{2} \tag{.1}$$

$$area(A) = \sqrt{s(s-s_1)(s-s_2)(s-s_3)} \tag{.2}$$

Appendix B: Global Nusselt number

The average Nusselt number can also be calculated from the energy balance in the dispersed phase. The heat transfer rate from dispersed phase to continuous phase can be given by Eq. .3 and Eq. .4. Here T_d is the average surface temperature of the dispersed phase and $T_{d,avg}$ is the average temperature of the dispersed phase averaged over it's whole volume.

$$\dot{q} = h_c A(T_d - T_c) \tag{.3}$$

$$\dot{q} = \frac{m_d C_{p_d} \Delta T_{d,avg}}{\Delta t} \tag{.4}$$

From the definition of Nusselt number i.e.,

$$Nu = \frac{h_c L}{\lambda_c} \tag{.5}$$

In Eq. .5, h_c can be replaced using Eq. .3 and Eq. .4. Also, λ_c can be written in terms of Re and Pr as,

$$\lambda_c = \frac{\rho_c C_{p_c} U L}{RePr} \tag{.6}$$

After replacing h_c and λ_c, the Nusselt number can be written as,

$$Nu_{global} = \left(\frac{\rho_d}{\rho_c}\right)\left(\frac{C_{p_d}}{C_{p_c}}\right)\left(\frac{\Delta T'_d}{\Delta t'}\right)\left(\frac{RePr}{6x}\right) \tag{.7}$$

where $\Delta T'_d$ and $\Delta t'$ represents dimensionless temperature change and dimensionless time step respectively. An important point to note here is that the temperature has been non-dimensionalized using $T_d - T_c$ where T_d is the average surface temperature and not the initial temperature of the dispersed phase. Here, the parameter x is used to represent the deviation in the area of the bubble from a perfect spherical geometry. It can be calculated by,

$$x = \frac{\text{bubble surface area}}{\text{surface area of a spherical bubble having the same volume}} \tag{.8}$$

Bibliography

[1] E. R. A. Coyajee. “A Front-Capturing Method for the Numerical Simulation of Dispersed Two-Phase Flow”. PhD thesis. TU Delft, 2007.

[2] M. Sussman and E. Puckett. “A coupled Level-Set and Volume-of-Fluid method for computing 3D and axisymmetric incompressible two-phase flows”. In: *J. Comp. Phys* 162 (2000), pp. 301–337.

[3] M. Kwakkel. “Numerical Modelling of turbulent dense dispersed two-phase flows”. PhD thesis. TU Delft, 2016.

[4] G. Batchelor. *An Introduction to Fluid Dynamics.* Cambridge University Press, United Kingdom, 1974.

[5] L. Landau and E. Lifshitz. *Fluid Mechanics, Second Edition.* Pergamon Press, 1987.

[6] M. Kang, R. Fedkiw, and X.D. Liu. “A boundary condition capturing method for multiphase incompressible flow”. In: *J. Sci. Comput.* 15 (2000), pp. 323–360.

[7] N. Talebanfard and B.J. Boersma. “Direct Numerical Simulation of Heat Transfer in Colliding Droplets by a Coupled Level Set and Volume of Fluid Method”. In: *Direct and Large-Eddy Simulation IX.* Ed. by J. Frohlich et al. Springer International Publishing, 2015, pp. 687–693.

[8] M.S. Dodd and A. Ferrante. “A fast pressure-correction method for incompressible two-fluid flows”. In: *Journal of Computational Physics* 273 (2014), pp. 416–434.

[9] S. Dong and J. Shen. “A time-stepping scheme involving constant coefficient matrices for phase-field simulations of two-phase incompressible flows with large density ratios”. In: *Journal of Computational Physics* 231.17 (2012), pp. 5788–5804.

[10] B.V. Leer. “Towards the Ultimate Conservative Difference Scheme. II. Monotonicity and Conservation combined in a Second-Order Scheme”. In: *Journal of Computational Physics* 14.4 (1974), pp. 361–370.

[11] X.D. Liu, R. Fedkiw, and M. Kang. “A Boundary Condition Capturing Method for Poisson’s Equation on Irregular Domains”. In: *Journal of Computational Physics* 160 (2000), pp. 151–178.

[12] H. Nemati, W.P. Breugem, and B.J. Boersma. “DNS of turbulent bubbly down flow using an efficient CLSVOF method”. In: *DLES11, Pisa* (2017).

[13] K.B. Deshpande and W.B. Zimmerman. “Simulation of interfacial mass transfer by droplet dynamics using the level set method”. In: *Chemical Engineering Science* 61 (2006), pp. 6486–6498.

[14] M. Hase and B. Weigand. “Numerical study of the temperature field of unsteady moving droplets and of the surrounding gas”. In: *Proceedings ILASS-Europe 2001, Zurich* (2001).

[15] M. Hase and B. Weigand. “Transient heat transfer of deforming droplets at high Reynolds numbers”. In: *International Journal of Numerical Methods for Heat and Fluid Flow* 14.1 (2004), pp. 85–97.

[16] R.F.L. Cerqueira, E.E. Paladino, and C.R. Maliska. “A computational study of the interfacial heat or mass transfer in spherical and deformed fluid particles flowing at moderate Re numbers”. In: *Chemical Engineering Science* 138 (2015), pp. 741–759.

[17] L. Oellrich, H. Schmidt-Traub, and H. Brauer. “Theoretische Berechnung des Stofftransports in der Umgebung einer Einzelblase”. In: *Chem. Eng. Sci* 28.3 (1973), pp. 711–721.

[18] R. Clift, J. Grace, and M. Weber. *Bubbles, Drops and Particles.* Academic Press, Inc., London, United Kingdom, 1978.

[19] S. P. Van Der Pijl. “Computation of Bubbly Flows with a Mass-Conserving Level-Set Method”. PhD thesis. TU Delft, 2005.

[20] K.L. Pan, C.K. Law, and B. Zhou. “Experimental and mechanistic description of merging and bouncing in head-on binary droplet collision”. In: *Journal of Applied Physics* 103.6 (2008).